



# The Relation between the Cool-core Radius and the Host Galaxy Clusters: Thermodynamic Properties and Cluster Mass

FanLam Ng<sup>1,2</sup> and Shutaro Ueda<sup>1,3</sup> <sup>1</sup> Academia Sinica Institute of Astronomy and Astrophysics (ASIAA), No. 1, Section 4, Roosevelt Road, Taipei 106216, Taiwan; [sueda@asiaa.sinica.edu.tw](mailto:sueda@asiaa.sinica.edu.tw)<sup>2</sup> Yuanpei College, Peking University, Yi He Yuan Road 5, Hai Dian District, Beijing 100871, People's Republic of China<sup>3</sup> Institute of Astronomy, National Tsing Hua University, Hsinchu 300044, Taiwan

Received 2023 September 28; revised 2024 April 12; accepted 2024 April 22; published 2024 June 10

## Abstract

We present a detailed study of cool-core systems in a sample of four galaxy clusters (RXCJ1504.1-0248, A3112, A4059, and A478) using archival X-ray data from the Chandra X-ray Observatory. Cool cores are frequently observed at the centers of galaxy clusters and are considered to be formed by radiative cooling of the intracluster medium (ICM). Cool cores are characterized by a significant drop in the ICM temperature toward the cluster center. We extract and analyze X-ray spectra of the ICM to measure the radial profiles of the ICM thermodynamic properties, including temperature, density, pressure, entropy, and radiative cooling time. We define the cool-core radius as the turnover radius in the ICM temperature profile and investigate the relation between the cool-core radius and the properties of the host galaxy clusters. In our sample, we observe that the radiative cooling time of the ICM at the cool-core radius exceeds 10 Gyr, with RXCJ1504.1-0248 exhibiting a radiative cooling time of  $32^{+5}_{-11}$  Gyr at its cool-core radius. These results indicate that not only radiative cooling but also additional mechanisms, such as gas sloshing, may play an important role in determining the size of cool cores. Additionally, we might find that the best-fit relation between the cool-core radius and the cluster mass ( $M_{500}$ ) is consistent with a linear relation. Our findings may suggest that cool cores are linked to the evolution of their host galaxy clusters.

*Unified Astronomy Thesaurus concepts:* [Galaxy clusters \(584\)](#); [Intracluster medium \(858\)](#); [X-ray astronomy \(1810\)](#)

## 1. Introduction

Galaxy clusters contain a large amount of diffuse, hot X-ray emitting gas known as the intracluster medium (ICM;  $T \sim 10^{7-8}$  K), which is trapped and thermalized in the deep gravitational potential well dominated by dark matter. Because of the high temperature of the ICM, the ICM emits X-ray radiation through thermal bremsstrahlung. Since the X-ray emissivity of the ICM is proportional to the square of the electron density, the ICM loses its thermal energy by X-ray radiation faster in the central region of galaxy clusters than in the outskirts.

The radiative cooling time of the ICM at the centers of galaxy clusters exhibiting strong X-ray surface brightness peaks is much shorter than the inferred age of galaxy clusters<sup>4</sup> (see, e.g., Peterson & Fabian 2006, for a review). Thus, it was expected that runaway cooling would occur and trigger massive star formation in the centers of galaxy clusters (Fabian 1994). However, this expectation is inconsistent with observational evidence. Neither such expected massive star formation nor a large amount of cooled ICM that serves as fuel for star formation is found (e.g., Tamura et al. 2001; Peterson et al. 2001; O’Dea et al. 2008; McDonald et al. 2011, 2018). This inconsistency indicates that runaway cooling must be suppressed, meaning the presence of heating sources.

Although a heating source is required, X-ray observations have revealed that the temperature of the ICM drops toward the

cluster center. The ICM temperature at the center is measured at a few keV, corresponding to 30%–50% of the peak value of the ICM temperature profile (e.g., Vikhlinin et al. 2005; Simionescu et al. 2011). Such a region, consisting of cooler ICM (or cooling ICM), is referred to as a cool core (Molendi & Pizzolato 2001). The presence of cool cores indicates that not only the cooling of the ICM is still dominant in cool cores but also the heating is balanced with the cooling of the ICM at least within a specific region. Therefore, exploring cool-core systems in galaxy clusters is important to understand not only the origin of cool cores but also the evolution of cool cores under conditions of the balance between cooling and heating.

Cool cores are characterized by a significant drop in the ICM temperature toward the cluster center (Molendi & Pizzolato 2001). However, various alternative observables of the ICM have been used to identify cool cores: central electron density (Hudson et al. 2010; Barnes et al. 2018), central radiative cooling time (e.g., Bauer et al. 2005; Hudson et al. 2010; Wang et al. 2023), central entropy profile (e.g., Bauer et al. 2005; Hudson et al. 2010), classical mass deposition rate (e.g., Chen et al. 2007), and X-ray luminosity ratio (e.g., Sayers et al. 2013; Shitanishi et al. 2018). These observables have also been used to distinguish between cool-core and non-cool-core clusters. For instance, Su et al. (2020) used the central radiative cooling time of the ICM as an indicator to identify cool-core clusters from a sample of galaxy clusters obtained from cosmological simulations such as IllustrisTNG. Additionally, Barnes et al. (2018) investigated the cool-core fraction in a sample of galaxy clusters from IllustrisTNG using six parameters: central electron density, radiative cooling time, entropy profile, X-ray concentration parameters within a certain or fiducial radius, and cuspsiness parameter of X-ray morphology. Laganá et al. (2019) also investigated the optimal parameters for identifying cool cores using some observables,

<sup>4</sup> 7.7 Gyr ( $z \sim 1$ ) is often adopted as the age of low- $z$  galaxy clusters.

including the cuspsiness of the gas density profile, central gas density, and properties of the brightest cluster galaxies (BCG).

Hudson et al. (2010) presented an in-depth study of the ICM properties in the central regions of galaxy clusters listed in a catalog of the extended HIGHEST X-ray FLUX Galaxy Cluster Sample (HIFLUGCS; Reiprich & Böhringer 2002). They applied 16 cool-core diagnostics parameters to their sample to find the most appropriate parameter for characterizing cool-core clusters. They found that the radiative cooling time at the center and cuspsiness serve as the most effective indicators for low- $z$  and high- $z$  cool-core clusters, respectively. In addition, they introduced two categories of cool cores: strong and weak cool cores, based on the radiative cooling time at the center. Strong cool cores are defined as those with a radiative cooling time at the center shorter than 1 Gyr, while weak cool cores are identified when a radiative cooling time ( $t_{\text{cool}}$ ) at the center falls within the range of 1 Gyr  $< t_{\text{cool}} < 7.7$  Gyr.

A universal form in the ICM temperature profile has been reported (e.g., Allen et al. 2001; Vikhlinin et al. 2005; Sanderson et al. 2006). Allen et al. (2001) analyzed the ICM temperature profiles scaled by  $r_{2500}$ <sup>5</sup> for six cool-core clusters and found an approximately universal form in the scaled temperature profiles. Vikhlinin et al. (2005) measured the ICM temperature profiles from the central region to the outskirts in 13 nearby, relaxed galaxy clusters and groups, and revealed a similar trend in the temperature profiles scaled by  $r_{180}$ . Sanderson et al. (2006) also measured the ICM temperature profiles in 20 galaxy clusters and found a possible universal form in the temperature profiles scaled by  $r_{500}$ .

Such previous studies aim to investigate possible relations between the temperature profile and the total mass of galaxy clusters. However, both cooling and heating processes have a significant impact on cool cores, indicating that baryon physics in the centers of galaxy clusters likely plays an important role in shaping the observed characteristics of cool cores. Therefore, it is essential to focus on cool-core systems and characterize cool cores by the ICM temperature.

In this paper, we aim to characterize cool cores in our sample using the cool-core radius, which is defined as the turnover radius in the ICM temperature profile. In addition, we aim to study possible relations between the cool-core radius and the properties of the host galaxy clusters, including the ICM thermodynamic properties and cluster mass. To this end, we first analyze the X-ray spectra of the ICM extracted from annular regions determined by the morphology of X-ray surface brightness and X-ray photon counts. Then, we measure the radial profiles of the ICM thermodynamic properties and determine the cool-core radius by analyzing the ICM temperature profile. Finally, we measure thermodynamic perturbations in the ICM to constrain the turbulent velocity of the ICM within the cool cores in our sample.

This paper is organized as follows. Section 2 provides a brief summary of our sample and their properties. Section 3 presents detailed information regarding Chandra observations and data reduction procedures. Section 4 describes the X-ray spectral analysis and measurements of the radial profiles of the ICM thermodynamic properties. Section 5 presents the study of possible relations between the cool-core radius and the properties of the host galaxy clusters and the analysis of

thermodynamic perturbations in the ICM. Finally, a summary is given in Section 6.

Throughout the paper, we assume  $\Omega_{\text{m}} = 0.3$ ,  $\Omega_{\Lambda} = 0.7$ , and the Hubble constant of  $H_0 = 70 \text{ km s}^{-1} \text{ Mpc}^{-1}$ . Unless stated otherwise, quoted errors correspond to  $1\sigma$  uncertainties.

## 2. Sample

In this paper, we focus on four galaxy clusters: RXCJ1504.1-0248, A3112, A4059, and A478. These galaxy clusters are included in the HIFLUGCS catalog (Reiprich & Böhringer 2002). According to Hudson et al. (2010), they are classified as strong cool-core clusters based on the radiative cooling time of the ICM at the center. From the sample of the strong cool-core clusters, these four clusters are selected based on (1) relatively hot gas (virial temperature of  $kT_{\text{vir}} > 4 \text{ keV}$ ; Hudson et al. 2010), (2) cooling, low-entropy gas at the center (cooling time of  $t_{\text{cool}} < 0.6 \text{ Gyr}$  or entropy of  $K_0 < 10 \text{ keV cm}^2$ ; Hudson et al. 2010), (3) high-contrast sloshing (all perturbations with entropy contrast of  $K_{\text{neg}}/K_{\text{pos}} > 1.3$ ; Ueda et al. 2021). Thus, they are characterized as relatively massive clusters hosting sloshing cool cores where a strong heating source(s) is required. Here, we provide a brief summary of previous studies on each galaxy cluster. The values of  $M_{500}$  and  $r_{500}$  mentioned below are extracted from the Meta-Catalog of X-ray-detected Clusters of galaxies (MCXC; Piffaretti et al. 2011).

### 2.1. RXCJ1504.1-0248

This cluster is located at a redshift of  $z = 0.2153$  and is known as one of the most massive galaxy clusters with  $M_{500} = 12.47 \times 10^{14} M_{\odot}$  ( $r_{500} = 1.52 \text{ Mpc}$ ). This cluster hosts an extremely cool core characterized by a short radiative cooling time (e.g., Böhringer et al. 2005; Hlavacek-Larrondo & Fabian 2011). Böhringer et al. (2005) analyzed the X-ray surface brightness profile using a  $\beta$ -model (Cavaliere & Fusco-Femiano 1976, 1978; Etti 2000) and found that the core radius of the  $\beta$ -model is  $\sim 30 h_{70}^{-1} \text{ kpc}$ <sup>6</sup>, which is significantly smaller than the cooling radius of  $\sim 140 \text{ kpc}$  which is defined as the position at a radiative cooling time of 10 Gyr. Furthermore, Böhringer et al. (2005) found a significant drop in the ICM temperature profile toward the cluster center. The ICM temperature at the center is measured to be below 5 keV, while the temperature of the ambient ICM is  $\sim 10.5 \text{ keV}$ . Hlavacek-Larrondo & Fabian (2011) reported that there is no obvious X-ray point source associated with the BCG. Giacintucci et al. (2011) found the presence of a radio mini-halo in the central region of this cluster.

### 2.2. A3112

This cluster is located at a redshift of  $z = 0.075$  and has a powerful radio source, PKS 0316-444, in the center. Takizawa et al. (2003) measured the radial profiles of the ICM thermodynamic properties, including temperature, abundance, electron density, pressure, and radiative cooling time with Chandra, and found a temperature drop toward the cluster center. Bulbul et al. (2012) also studied the temperature profile of the ICM from the center to the outskirts. The ICM temperature at the center is measured at  $\sim 3.4 \text{ keV}$ , while the peak value in the temperature profile is measured at  $\sim 5.1 \text{ keV}$ , which is consistent

<sup>5</sup> We adopt  $M_{\Delta}$  as the mass enclosed within a sphere of radius  $r_{\Delta}$  whose mean density is  $\Delta$  times the critical density of the Universe at the redshift of the galaxy cluster.

<sup>6</sup>  $h_{70}$  denotes  $h_{70} = H_0 / (70 \text{ km s}^{-1} \text{ Mpc}^{-1})$  where  $H_0$  is a Hubble constant used in the literature.

**Table 1**  
Summary of Our Sample: Cluster Name, Redshift, Net Exposure Time, Physical Scale, and Data Sets Taken with Chandra

Cluster	Redshift	Exp. Time (ks)	Scale (kpc arcsec <sup>-1</sup> )	ObsID
RXCJ1504.1-0248	0.215	161.7	3.51	4935, 5793, 17197, 17669, 17670
A3112	0.075	133.7	1.43	2216, 2516, 6972, 7323, 7324, 13135
A4059	0.049	120.0	0.96	897, 5785
A478	0.088	50.1	1.65	1669, 6102

with that reported by Ezer et al. (2017). The mass of this cluster is estimated at  $M_{500} = 4.39 \times 10^{14} M_{\odot}$  ( $r_{500} = 1.13$  Mpc), which is consistent with that estimated by Nulsen et al. (2010) and Bulbul et al. (2012).

### 2.3. A4059

This cluster is located at a redshift of  $z = 0.049$ . The ICM temperature profile shows a temperature drop from  $\sim 4$  keV at  $\sim 100$  kpc away from the center to  $\sim 2$  keV at the center (e.g., Huang & Sarazin 1998; Choi et al. 2004; Reynolds et al. 2008; Mernier et al. 2015). Laganá et al. (2019) conducted a detailed study of spatial distributions of the ICM temperature, entropy, pressure, and abundance, respectively. The mass of this cluster is estimated as  $M_{500} = 2.67 \times 10^{14} M_{\odot}$  ( $r_{500} = 0.96$  Mpc), which is consistent with that estimated by Vikhlinin et al. (2009). Reynolds et al. (2008) reported a slight dip in the pressure profile at  $r \sim 15$  kpc, which is likely associated with an X-ray cavity caused by active galactic nuclei (AGN) feedback. Thus, it is considered that a lack of thermal pressure may be supported by its nonthermal pressure.

### 2.4. A478

This cluster is located at a redshift of  $z = 0.088$ . Sun et al. (2003) analyzed the central 500 kpc region with Chandra and reported the radial profiles of the ICM thermodynamic properties, finding that the peak value in the temperature profile is  $\sim 8.5$  keV, while the temperature at the center is  $\sim 3$  keV. These results are in agreement with those measured by Pointecouteau et al. (2004) and Vikhlinin et al. (2005). X-ray cavities are observed in the central 15 kpc region, with two weak and small ( $\sim 4$  kpc) radio lobes spatially associated with the X-ray cavities (Sun et al. 2003). The mass of this cluster is estimated as  $M_{500} = 6.42 \times 10^{14} M_{\odot}$  ( $r_{500} = 1.28$  Mpc).

## 3. Observation and Data Reduction

We analyzed archival X-ray data of the sample taken with the Advanced CCD Imaging Spectrometer (ACIS; Garmire et al. 2003) on board the Chandra X-ray Observatory. This paper employs a list of Chandra data sets, obtained by the Chandra X-ray Observatory.<sup>7</sup> The observation identification numbers (ObsIDs) and corresponding information of Chandra observations in this study are summarized in Table 1. We used versions 4.11 and 4.8.3 for the Chandra Interactive Analysis of Observations (CIAO; Fruscione et al. 2006) and the calibration database (CALDB), respectively. To ensure data quality, we examined the light curve of each data set using the `lc_clean` task in CIAO, filtering flare data. The `blanksky` data provided by CALDB were adopted as background data for the spectral analysis. Point sources were identified by the `wavdetect` task

in CIAO and were subsequently masked. We extracted X-ray spectra of the ICM from each data set using the `specextract` task in CIAO and combined them after making individual spectrum, response, and ancillary response files for the spectral fitting. We used XSPEC version 12.11.0f (Arnaud 1996) and the atomic database (AtomDB) for plasma emission modeling version 3.0.9 in the X-ray spectral analysis, assuming that the ICM is in collisional ionization equilibrium (Smith et al. 2001; Foster et al. 2012). The abundance table of Anders & Grevesse (1989) was used in XSPEC. Here, the abundance of a given element is defined as  $Z_i = (n_{i,\text{obs}}/n_{\text{H, obs}})/(n_{i,\odot}/n_{\text{H},\odot})$ , where  $n_i$  and  $n_{\text{H}}$  represent the number densities of the  $i$ th element and hydrogen, respectively. The iron abundance of the ICM is used to represent the ICM metal abundance, such that the abundance of other elements is tied to the iron abundance as  $Z_i = Z_{\text{Fe}}$  (Ueda et al. 2021).

## 4. Analysis and Results

To determine the cool-core radius for the sample, our initial goal is to obtain and analyze the ICM temperature profile of each cluster. We define annular regions for X-ray spectral analysis based on the morphology of the X-ray surface brightness of the sample. Next, we extract X-ray spectra of the ICM from each defined annular region and carry out spectral analysis to measure the ICM thermodynamic properties. Then, we perform a fitting of the ICM temperature profile to determine the cool-core radius. We also study the radial profiles of the ICM electron number density, pressure, entropy, and radiative cooling time.

### 4.1. X-Ray Imaging Analysis

Figure 1 shows the X-ray surface brightness images of the sample in the 0.5–7.0 keV band taken with Chandra after subtracting the background and correcting the exposure time. Since the morphology of their X-ray surface brightness appears axial symmetric (e.g., Ueda et al. 2021). We adopt the same elliptical model as that used in Ueda et al. (2021) to define annular regions for spectral analysis. The position of the center, the position angle (PA), and the axis ratio (AR) of the elliptical model for each cluster are summarized in Table 2. Note that Ueda et al. (2021) calculated a mean surface brightness by applying the concentric ellipse fitting algorithm constructed by Ueda et al. (2017), by minimizing the variance of the X-ray surface brightness relative to the ellipse model. To determine the width of each radial bin, we ensure that the net photon counts for each bin falls within the range of 5000–10,000 in the 0.4–7.0 keV band for better statistics. For several smaller regions near the center and outer regions, we adjust the net photon counts in the range of 1500–5000. The detailed information regarding our region selection is summarized in Appendix A (see Table 10).

<sup>7</sup> doi:10.25574/cdc.223

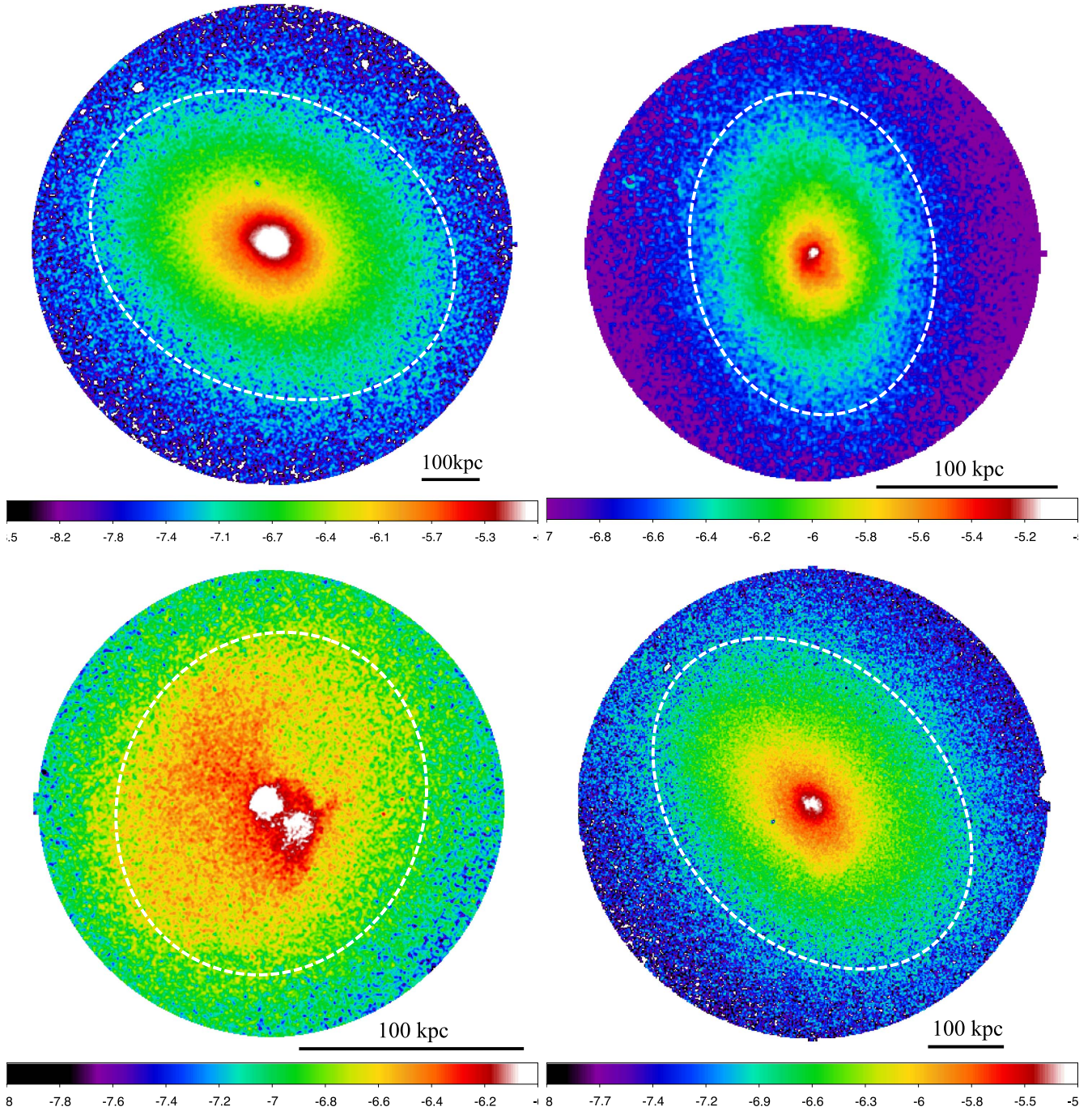


**Figure 1.** X-ray surface brightness of the sample: RXCJ1504.1-0248 (top left), A3112 (top right), A4059 (bottom left), and A478 (bottom right). The X-ray surface brightness in the 0.5–7.0 keV band is shown on a logarithm scale in units of  $\text{photon sec}^{-1} \text{arcsec}^{-2} \text{cm}^{-2}$ . This image is smoothed with a Gaussian kernel with a  $2\frac{2}{3}$  FWHM. A dashed, white ellipse shows the cool-core radius,  $r_{\text{cool}}$ , derived from the best-fit results of the analysis of the ICM temperature profile.

#### 4.2. X-Ray Spectral Analysis

We extract X-ray spectra of the ICM from each elliptical annulus defined in Section 4.1. The X-ray spectra in the 0.4–7.0 keV band are analyzed using the model of `phabs*apec` in `XSPEC`. The redshift of each cluster is fixed to the value in Table 1, which is taken from the NASA/IPAC Extragalactic Database.<sup>8</sup> The column densities of the Galactic absorption (i.e.,  $N_{\text{H}}$ ) toward RXCJ1504.1-0248 and A3112 are fixed to the

values measured by HI4PI Collaboration et al. (2016), respectively. However, for A4059 and A478, Choi et al. (2004) and Sun et al. (2003) reported that  $N_{\text{H}}$  varies with radius and is systematically larger than that derived from HI4PI Collaboration et al. (2016). In fact, the measured values of  $N_{\text{H}}$  for A4059 and A478 in our spectral analysis are a factor of 2 larger than those of HI4PI Collaboration et al. (2016), respectively, and consistent with the previous measurements (Sun et al. 2003; Choi et al. 2004), respectively. Therefore, we allow  $N_{\text{H}}$  for A4059 and A478 to vary in the spectral analysis.

<sup>8</sup> <http://ned.ipac.caltech.edu/>

**Table 2**

Sky Coordinates (J2000.0) of the Center, the PA, and the AR of the Ellipse Model for the X-Ray Surface Brightness Distribution of the Sample Extracted from Ueda et al. (2021)

Cluster	R.A.	Decl.	PA <sup>a</sup> (deg)	AR
RXCJ1504.1-0248	15 <sup>h</sup> 04 <sup>m</sup> 07 <sup>s</sup> .48	−02°48′17″.25	156	0.78
A3112	03 <sup>h</sup> 17 <sup>m</sup> 57 <sup>s</sup> .67	−44°14′17″.44	100	0.75
A4059	23 <sup>h</sup> 57 <sup>m</sup> 00 <sup>s</sup> .79	−34°45′33″.44	70	0.88
A478	04 <sup>h</sup> 13 <sup>m</sup> 25 <sup>s</sup> .15	10°27′54″.94	132	0.73

**Note.**

<sup>a</sup> PA measured south of east.

The observed radial profiles of the temperature and electron number density for the sample are shown in Figures 2 and 3, respectively. To estimate the ICM electron number density, we assume a line-of-sight length of  $L/1$  Mpc. Additionally, the observed radial profiles of the ICM metal abundance are presented in Appendix (Figure 10). We also calculate the ICM pressure  $p_e$  and entropy  $K_e$  as

$$p_e = kT \times n_e \quad (1)$$

and

$$K_e = kT \times n_e^{-\frac{2}{3}}, \quad (2)$$

respectively, where  $kT$  is the ICM temperature and  $n_e$  is the ICM electron number density. The radial profiles of the pressure and entropy are shown in Figures 4 and 5, respectively. In addition, following the approach of McDonald et al. (2019), we calculate the radiative cooling time of the ICM,  $t_{\text{cool}}$ , as

$$t_{\text{cool}} = \frac{3(n_e + n_p)kT}{2n_en_p\Lambda(T, Z)}, \quad (3)$$

where  $n_p$  is the proton number density, and  $\Lambda(T, Z)$  is the cooling function. To convert from  $n_en_p$  to  $n_e$ , McDonald et al. (2019) assumed  $n_e/n_p = 1.196$ , based on the discussion by Markevitch (2007), namely,  $n_e/n_p = 1 + 2x + x_{\text{eh}}$ , where  $x \equiv n_{\text{He}}/n_p$  represents the helium abundance, and  $x_{\text{eh}}$  represents electrons from elements heavier than helium. The contribution of  $x_{\text{eh}}$  can be negligible, as it is  $x_{\text{eh}} \approx 0.005$ , assuming an ICM abundance of 0.3–0.5 solar compared to  $x = 0.098$  from Anders & Grevesse (1989), with 1 solar abundance. Therefore, we adopt the same approach as McDonald et al. (2019) in the calculation of the radiative cooling time. We compute the cooling function using the `pyatomdb` task in `AtomDB` (Smith et al. 2001; Foster et al. 2012) with the best-fit parameters of the ICM temperature and abundance in each radial bin. The radial profiles of the radiative cooling time for the sample are presented in Figure 6. To show all the radial profiles, we use the distance from the center along the direction of the major axis of the elliptical model as the values on the horizontal axis.<sup>9</sup> Note that we here show the radial profiles of the ICM properties derived from projected spectral analysis, not spectral deprojection analysis.

<sup>9</sup> In this paper, we adopt  $r = \frac{r_{\text{MAJ, inner}} + r_{\text{MAJ, outer}}}{2}$  as the distance from the center, where  $r_{\text{MAJ, inner}}$  and  $r_{\text{MAJ, outer}}$  denote the major axes of the inner and outer annuli, respectively.

### 4.3. ICM Temperature Profiles

Figure 2 shows the observed temperature profile of each galaxy cluster. In good agreement with previous studies, such as those of Bohringer et al. (2005) for RXCJ1504.1-0248, Takizawa et al. (2003) for A3112, Reynolds et al. (2008) for A4059, and Sanderson et al. (2005) for A478. All galaxy clusters in the sample exhibit a significant drop in the observed ICM temperature profiles toward the cluster center.

Several empirical models have been proposed to represent the ICM temperature profile from the center to the outskirts (e.g., Allen et al. 2001; Voigt et al. 2002; Kaastra et al. 2004; Vikhlinin et al. 2006; O’Sullivan et al. 2017). For instance, Kaastra et al. (2004) modeled the ICM temperature profile, taking into account the temperature at the center, the peak temperature, and the cooling radius that represents a characteristic radius in the temperature profile. However, there is still room for improvement in their model to account for a temperature decrease toward the outskirts.

Motivated by Kaastra et al. (2004) and O’Sullivan et al. (2017), we extend their models to account for the temperature profile from the center to the outer region. Therefore, our model can be described as

$$T(r) = T_{\text{center}} + 2 \times (T_{\text{peak}} - T_{\text{center}}) \left( \frac{x(r)}{1 + x(r)} \right) \quad (4)$$

$$x(r) = \begin{cases} (r/r_{\text{cool}})^{\alpha_1} & : r < r_{\text{cool}} \\ (r/r_{\text{cool}})^{\alpha_2} & : r \geq r_{\text{cool}}, \end{cases} \quad (5)$$

where  $T_{\text{center}}$  is the ICM temperature at the center,  $T_{\text{peak}}$  is the peak temperature,  $r_{\text{cool}}$  is the turnover radius in the temperature profile (i.e., the peak position;  $T(r_{\text{cool}}) = T_{\text{peak}}$ ), and  $\alpha_1$  and  $\alpha_2$  represent the slopes of the temperature profile within  $r_{\text{cool}}$ , and beyond  $r_{\text{cool}}$ , respectively. In this paper, we define the cool-core radius as  $r_{\text{cool}}$ .

We fit the observed temperature profile shown in Figure 2 with our model using affine-invariant Markov Chain Monte Carlo (MCMC) sampling (Goodman & Weare 2010) implemented by the `emcee` Python package (Foreman-Mackey et al. 2013). The log-likelihood function for the fitting is written as

$$-2 \ln \mathcal{L} = \sum_i \frac{[y_i - T(r_i)]^2}{\sigma_{y_i}^2}, \quad (6)$$

where  $i$  runs over all radial bins in the radial profile,  $y_i$  and  $\sigma_{y_i}$  are the best-fit value and its uncertainty of the temperature profile in each radial bin, respectively, and  $T(r_i)$  is the model prediction in each radial bin. We use uninformative uniform priors on  $T_{\text{center}}$ ,  $T_{\text{peak}}$ ,  $r_{\text{cool}}$ ,  $\alpha_1$ , and  $\alpha_2$  with the following ranges:  $T_{\text{center}} \in (0, 30)$  keV,  $T_{\text{peak}} \in (0, 30)$  keV,  $r_{\text{cool}} \in (0, 500)$  kpc,  $\alpha_1 \in (0, 2)$ , and  $\alpha_2 \in (-2, 0)$ . We sample the posterior probability distributions of the parameters ( $T_{\text{center}}$ ,  $T_{\text{peak}}$ ,  $r_{\text{cool}}$ ,  $\alpha_1$ , and  $\alpha_2$ ) over the full parameter space allowed by the priors. The mean value and standard deviation of the marginalized distributions are represented as the best-fit value and its uncertainty, respectively. For each cluster, the best-fit parameters of the temperature profile are summarized in Table 3. The best-fit model of the temperature profile of each cluster is also shown in Figure 2.

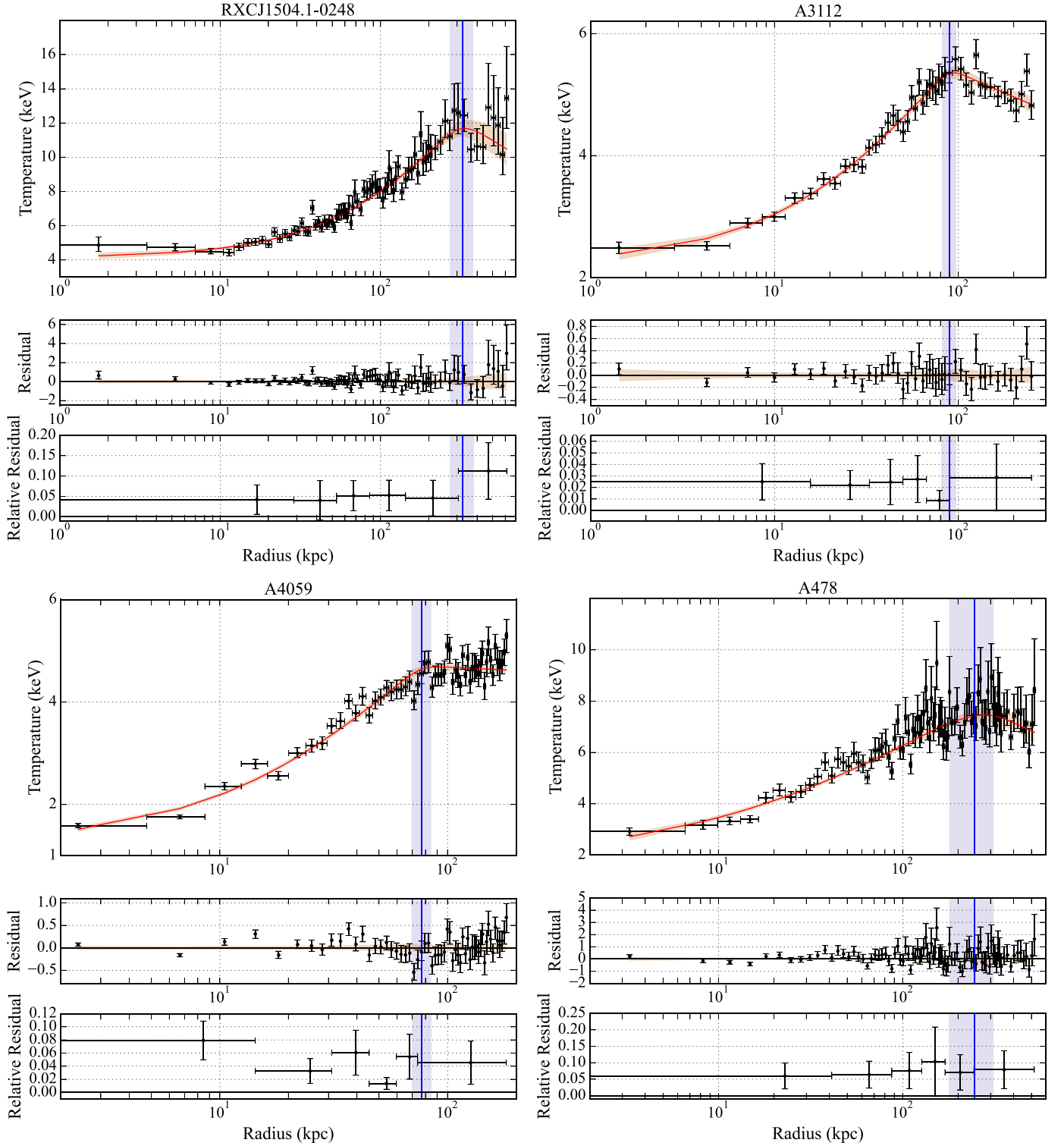


**Figure 2.** ICM temperature profiles of the sample: RXCJ1504.1-0248 (top left), A3112 (top right), A4059 (bottom left), and A478 (bottom right). In each panel, the black error bars show the observed values. The red dashed line and shaded region display the best-fit profile and  $1\sigma$  uncertainty, respectively. The blue solid line and shaded region correspond to the best-fit cool-core radius  $r_{\text{cool}}$  and  $1\sigma$  uncertainty, respectively. In the middle row of each panel, the residuals between the observed and the best-fit profiles are shown. The mean absolute relative residuals are also displayed in the bottom row of each panel.

We calculate residuals between the observed and the best-fit profiles in each radial bin. The residuals are computed as  $(y_i - T_b(r_i))$ , where  $T_b(r_i)$  is the best-fit profile in each radial bin. Based on these residuals, we also compute the mean absolute relative residual within each set of five radial bins within  $r_{\text{cool}}$  as well as for all the data points for

the outer region (i.e.,  $r > r_{\text{cool}}$ ) using  $|(y - T_b)/T_b|$ . The profiles of the residuals and the mean absolute relative residuals are shown in the middle and bottom row of each panel in Figure 2, respectively. The calculation of residuals will also be applied to the radial profiles of the other components.

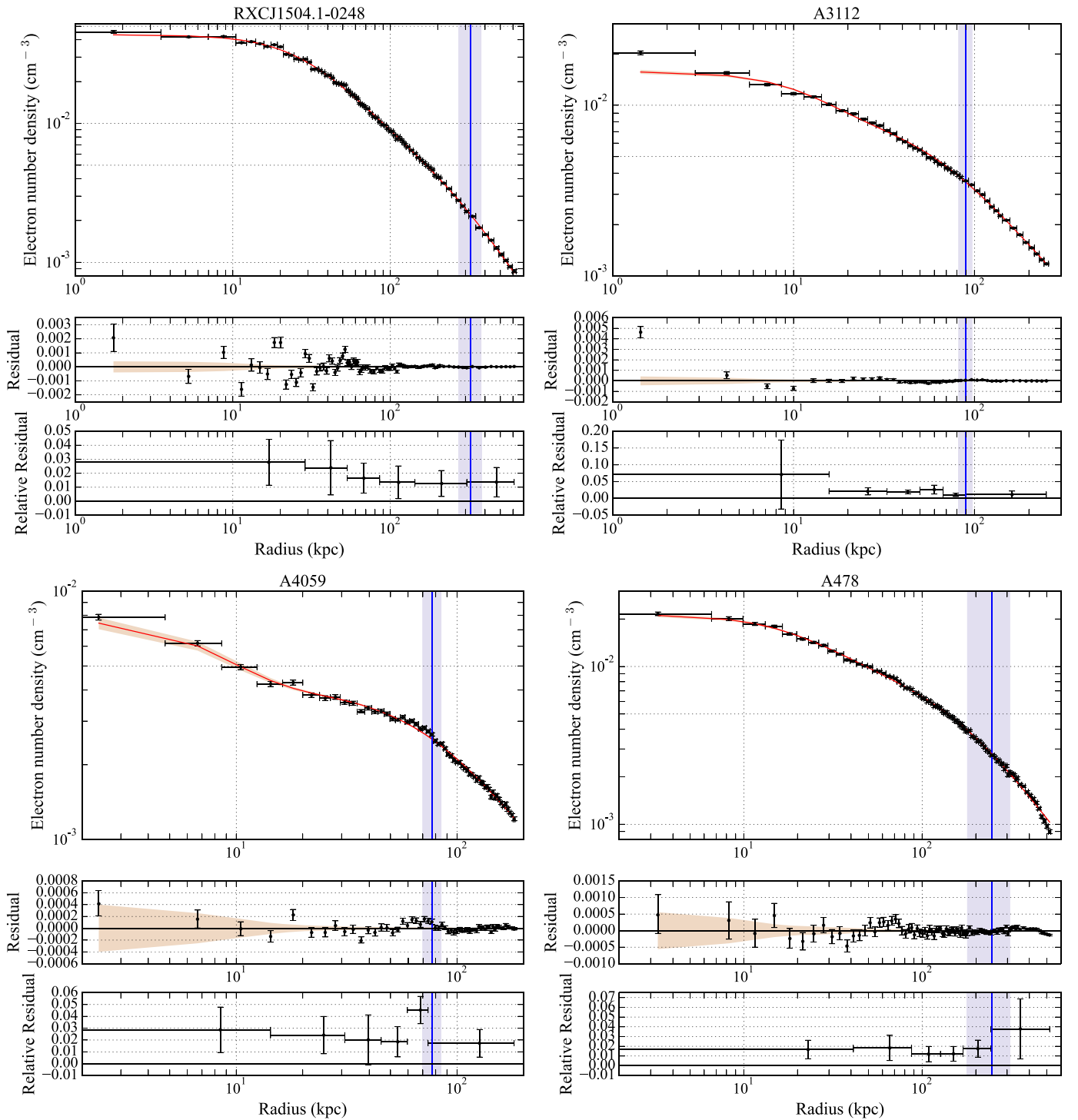


**Figure 3.** Same as Figure 2 but for the ICM electron number density profiles of the sample: RXCJ1504.1-0248 (top left), A3112 (top right), A4059 (bottom left), and A478 (bottom right).

We also calculate the ratios of the parameters of the temperature profile for RXCJ1504.1-0248, A3112, and A478 to those for A4059 since A4059 has the smallest values for each parameter. These ratios are summarized in Table 4.

#### 4.4. ICM Electron Number Density Profiles

In the same manner as the analysis of the ICM temperature profiles, we also analyze the radial profiles of the electron

number density for the sample. A  $\beta$ -model is frequently used to model the density profile of the ICM (e.g., Cavaliere & Fusco-Femiano 1976, 1978; Ettori 2000). For cool-core clusters, a double  $\beta$ -model is preferred to account for the observed profile because of the strong excess at the cluster center (e.g., Pointecouteau et al. 2004; Santos et al. 2008; Henning et al. 2009; Santos et al. 2010; Ota et al. 2013). Therefore, to fit the observed number density profile for each cluster, we adopt a

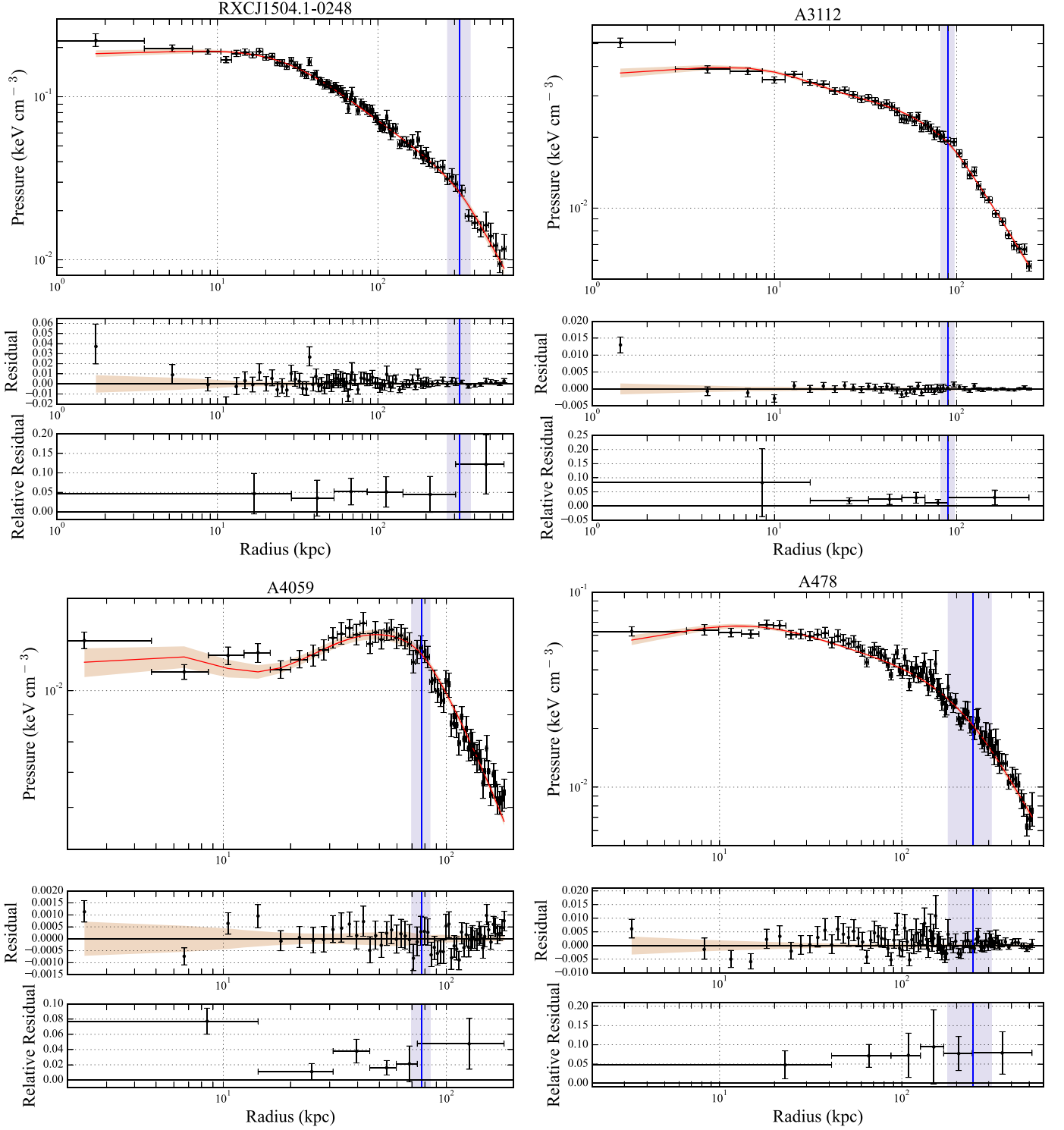


**Figure 4.** Same as Figure 3 but for the ICM pressure profiles of the sample: RXCJ1504.1-0248 (top left), A3112 (top right), A4059 (bottom left), and A478 (bottom right).

double- $\beta$ -model expressed as

$$\begin{aligned}
 n(r) &= n_1(r) + n_2(r) \\
 &= n_{0,1} \left[ 1 + \left( \frac{r}{r_{c,1}} \right)^2 \right]^{-\alpha_1} + n_{0,2} \left[ 1 + \left( \frac{r}{r_{c,2}} \right)^2 \right]^{-\alpha_2}, \quad (7)
 \end{aligned}$$

where  $n_{0,1}$  and  $n_{0,2}$  represent the values at the center, respectively,  $r_{c,1}$  and  $r_{c,2}$  are the core radii of each  $\beta$ -model, respectively, and  $\alpha_1$  and  $\alpha_2$  are the slopes of each  $\beta$ -model, respectively.

Following the procedures of the MCMC analysis in Section 4.3, we use uninformative uniform priors  $n_{0,1}$ ,

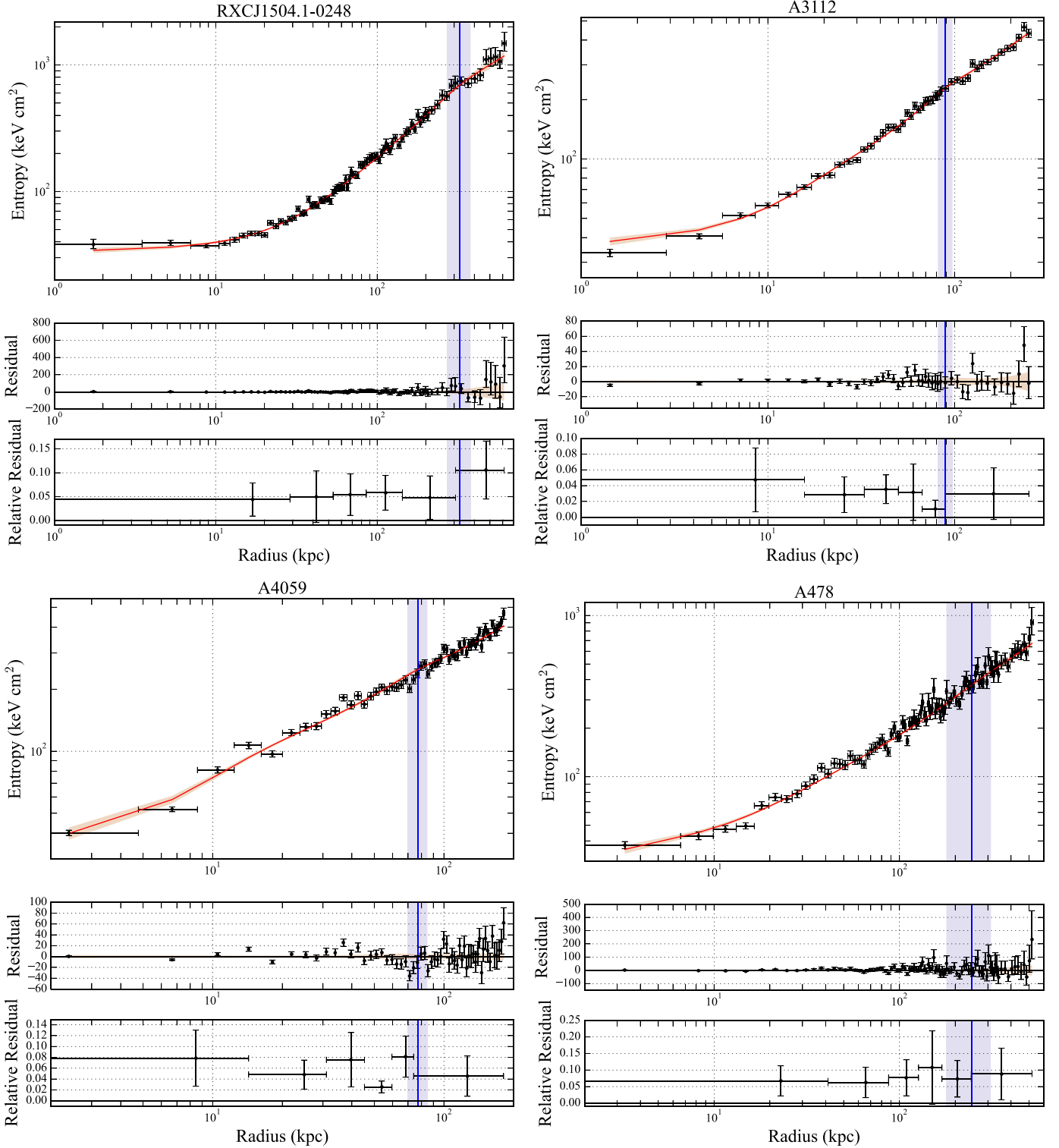


**Figure 5.** Same as Figure 3 but for the ICM Entropy profiles of the sample: RXCJ1504.1-0248 (top left), A3112 (top right), A4059 (bottom left), and A478 (bottom right).

$n_{0,2} \in (0, 1) \text{ cm}^{-3}$ ,  $r_{c,1}, r_{c,2} \in (0, 1000) \text{ kpc}$ ,  $\alpha_1, \alpha_2 \in (0.5, 3.5]$ , and ensure  $n_{0,1} > n_{0,2}$ . Thus, we fit the observed profile and sample the posterior probability distributions of these six parameters over the full parameter space allowed by the priors. The best-fit parameters obtained from the MCMC analysis are summarized in Table 5. The best-fit profile of each cluster, along with its uncertainty, is shown in Figure 3.

#### 4.5. ICM Pressure and Entropy Profiles

Based on the best-fit profiles for the ICM temperature and electron number density, we compute the predicted profiles for the ICM pressure and entropy profiles using Equations (1) and (2), respectively. Here, we do not perform direct fitting of the ICM pressure and entropy profiles. The observed ICM pressure

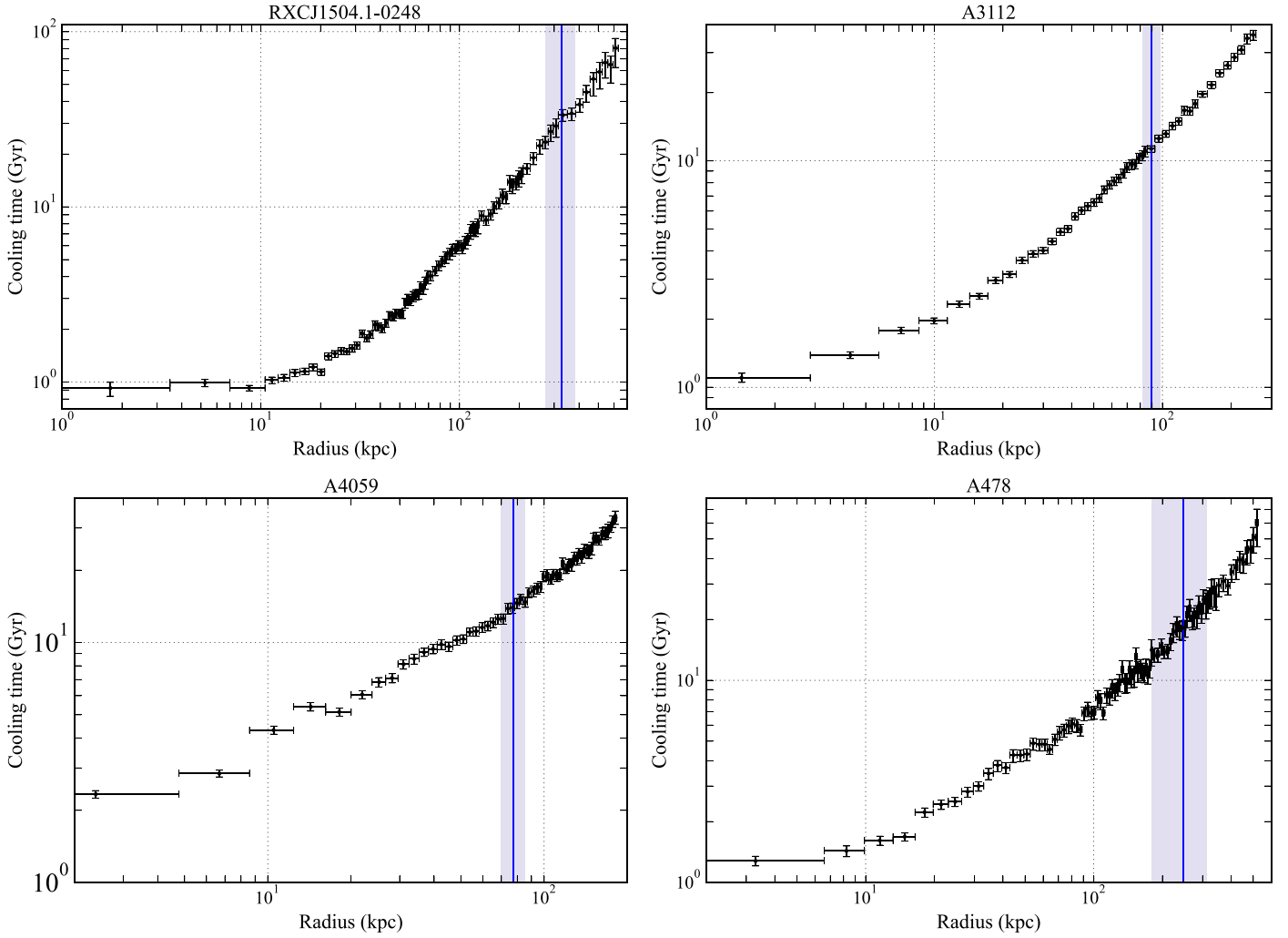


**Figure 6.** Radial profiles of the ICM radiative cooling time: RXCJ1504.1-0248 (top left), A3112 (top right), A4059 (bottom left), and A478 (bottom right). The blue, vertical solid line and shaded region correspond to the cool-core radius and  $1\sigma$  uncertainty for each cluster.

**Table 3**  
Parameter Constraints of the Temperature Profile Model Derived from the MCMC Analysis

Cluster	$T_{\text{center}}$ (keV)	$T_{\text{peak}}$ (keV)	$r_{\text{cool}}$ (kpc)	$\alpha_1$	$\alpha_2$
RXCJ1504.1-0248	$4.13 \pm 0.24$	$12.00 \pm 0.56$	$325 \pm 55$	$0.97 \pm 0.11$	$-0.66 \pm 0.48$
A3112	$2.21 \pm 0.16$	$5.41 \pm 0.11$	$89.4 \pm 8.0$	$0.88 \pm 0.10$	$-0.35 \pm 0.14$
A4059	$1.21 \pm 0.13$	$4.70 \pm 0.08$	$77.1 \pm 8.7$	$0.90 \pm 0.10$	$-0.05 \pm 0.05$
A478	$1.54 \pm 0.65$	$7.62 \pm 0.32$	$245 \pm 66$	$0.55 \pm 0.13$	$-0.45 \pm 0.42$

**Table 4**  
Ratios of the Parameters of the Temperature Profile for RXCJ1504.1-0248, A3112, and A478 to Those of A4059

Cluster	$T_{\text{center}}/T_{\text{center,A4059}}$	$T_{\text{peak}}/T_{\text{peak,A4059}}$	$r_{\text{cool}}/r_{\text{cool,A4059}}$
RXCJ1504.1-0248	$3.42 \pm 0.42$	$2.55 \pm 0.13$	$4.21 \pm 0.82$
A3112	$1.83 \pm 0.24$	$1.15 \pm 0.03$	$1.16 \pm 0.16$
A478	$1.27 \pm 0.55$	$1.62 \pm 0.07$	$3.18 \pm 0.92$

and entropy profiles and their predicted profiles are shown in Figures 4 and 5, respectively.

As mentioned in Section 2.3, Reynolds et al. (2008) observed a slight dip in the pressure profile of A4059 at

$r \sim 15$  kpc. We also observe this dip in our pressure profile, which is in agreement with that reported by Reynolds et al. (2008). The X-ray cavity found by Reynolds et al. (2008) may be associated with this pressure dip and give nonthermal pressure support for this region.

## 5. Discussion

We have conducted an analysis of the radial profiles of the ICM thermodynamic properties, including temperature, electron number density, pressure, entropy, and radiative cooling time for our sample: RXCJ1504.1-0248, A3112, A4059, and A478. We have also determined the cool-core radius for each cluster by analyzing their observed ICM temperature profiles.

**Table 5**  
Parameter Constraints of the Double  $\beta$ -model Derived from the MCMC Analysis

Cluster	$n_{0,1}$ ( $10^{-2} \text{ cm}^{-3}$ )	$r_{c,1}$ (kpc)	$\alpha_1$	$n_{0,2}$ ( $10^{-2} \text{ cm}^{-3}$ )	$r_{c,2}$ (kpc)	$\alpha_2$
RXCJ1504.1-0248	$4.10 \pm 0.15$	$30.0 \pm 2.0$	$0.72 \pm 0.08$	$0.24 \pm 0.12$	$329 \pm 111$	$1.71 \pm 0.83$
A3112	$0.80 \pm 0.02$	$53.9 \pm 2.6$	$0.62 \pm 0.01$	$0.78 \pm 0.03$	$19.1 \pm 2.9$	$2.16 \pm 0.39$
A4059	$0.40 \pm 0.01$	$72.5 \pm 4.6$	$0.60 \pm 0.03$	$0.38 \pm 0.04$	$14.7 \pm 8.8$	$2.86 \pm 0.51$
A478	$1.54 \pm 0.09$	$19.8 \pm 2.1$	$0.64 \pm 0.10$	$0.59 \pm 0.08$	$161 \pm 17$	$0.85 \pm 0.08$

**Table 6**  
Cool-core Radius, Cluster Mass  $M_{500}$ , Fiducial Radius  $r_{500}$ , and Those Scaled by the Values of A4059

Cluster	$r_{\text{cool}}$ (kpc)	$r_{\text{cool}}/r_{\text{cool,A4059}}$	$r_{500}$ (Mpc)	$r_{\text{cool}}/r_{500}$	$r_{500}/r_{500,A4059}$	$M_{500}$ ( $10^{14} M_{\odot}$ )	$M_{500}/M_{500,A4059}$
RXCJ1504.1-0248	$325 \pm 55$	$4.21 \pm 0.82$	1.52	$0.21 \pm 0.04$	1.58	12.47	4.68
A3112	$89.4 \pm 8.0$	$1.16 \pm 0.16$	1.13	$0.080 \pm 0.007$	1.17	4.39	1.65
A4059	$77.1 \pm 7.7$	1.00	0.96	$0.080 \pm 0.008$	1.00	2.67	1.00
A478	$245 \pm 66$	$3.18 \pm 0.92$	1.28	$0.19 \pm 0.05$	1.32	6.42	2.41

In this section, we discuss the characteristics of the cool-core systems defined by the cool-core radius in the sample. We also explore possible relations between the cool-core radius and the properties of the host galaxy clusters, as well as investigate potential universal forms in the radial profiles scaled by the cool-core radius. Furthermore, we study perturbations in the ICM thermodynamic properties within the cool cores.

### 5.1. Cool-core Radius

Cool cores are characterized by a significant drop in the ICM temperature toward the cluster center (Molendi & Pizzolato 2001). Since the cool-core radius has been defined as the turnover radius in the ICM temperature profile, the cool-core radius corresponds to a boundary region where the cooling of the ICM becomes dominant. Therefore, the cool-core radius is an important aspect for understanding the underlying physics of cool cores.

We have determined the cool-core radius for the sample, as summarized in Table 3. Among our sample, RXCJ1504.1-0248 has the largest cool-core radius ( $r_{\text{cool}} = 324 \pm 55$  kpc), while A4059 has the smallest cool-core radius ( $r_{\text{cool}} = 77 \pm 8$  kpc). A3112 and A478 exhibit a relatively small and large cool-core radii, respectively.

We find that the radiative cooling time of the ICM at the cool-core radius exceeds 10 Gyr for all galaxy clusters in our sample (see Figure 6). In particular, RXCJ1504.1-0248 exhibits a radiative cooling time of  $32_{-11}^{+5}$  Gyr at its cool-core radius. These timescales are significantly longer than the inferred age of low- $z$  galaxy clusters. Our results indicate that the ICM temperature starts dropping toward the cluster center from a region exhibiting such a long radiative cooling time. Although it is difficult to predict the past thermodynamic properties of the ICM at the same region as the present cool-core radius, it is expected that the effect of radiative cooling in such regions is minimal or negligible. Furthermore, our results show that the radiative cooling time of the ICM gradually increases toward the outskirts, indicating no apparent feature or discontinuity at the cool-core radius. Therefore, our findings indicate that mechanisms for determining the size of cool cores rely not only on radiative cooling but also on additional mechanisms.

Gas sloshing can induce displacement of cool gas originally in a cool core toward the outskirts, leading to the mixing of

cool gas with ambient hot gas (e.g., Ascasibar & Markevitch 2006; ZuHone et al. 2010; Keshet 2012; Naor & Keshet 2020; Keshet et al. 2023). Since the cool-core systems in the sample have developed well, as indicated by the observed temperature drop, radiative cooling is expected to play a dominant role in generating cool gas in the inner regions of the cool cores. Such cool gas is likely to be displaced toward the outer regions by gas sloshing. In fact, evidence of gas sloshing has been observed in the cool cores in our sample (Ueda et al. 2021), supporting this hypothesis.

### 5.2. Relation between the Cool-core Radius and the Cluster Mass

To explore possible relations between the cool-core radius and the cluster mass, we extract the  $M_{500}$  and  $r_{500}$  values for our sample from the MCXC catalog (Piffaretti et al. 2011). These values are summarized in Table 6. Since  $r_{500}$  is commonly used as a scaling factor for the radial profiles of the ICM thermodynamic properties, this study provides insights into the connection between the cool-core radius and  $r_{500}$ .

To investigate the relations of the cool-core radius to  $M_{500}$  and to  $r_{500}$ , we conduct a regression analysis using a model expressed as

$$\frac{r_{\text{cool}}}{\hat{r}_{\text{cool}}} = N_i \left( \frac{x_i}{\hat{x}_i} \right)^{\alpha_i}, \quad (8)$$

where  $N_i$  is a normalization of the model defined as  $N_i = 10^{A_i}$ ,  $x_i$  represents either  $M_{500}$  or  $r_{500}$ , and  $\alpha_i$  is the slope of the model. Here,  $i$  denotes the values for  $M_{500}$  or  $r_{500}$ . We center the relation on the pivot values  $\hat{r}_{\text{cool}} = 167$  kpc,  $\hat{M}_{500} = 5.41 \times 10^{14} M_{\odot}$ , and  $\hat{r}_{500} = 1.20$  Mpc set at the median of the distributions of  $r_{\text{cool}}$ ,  $M_{500}$ , and  $r_{500}$ , respectively.

Following the procedures of the MCMC analysis in Section 4.3, we use uninformative uniform priors  $A_r, A_M \in (-5, 5)$  and  $\alpha_r, \alpha_M \in (0, 10)$ . We fit the data in the log-log space and sample the posterior probability distributions of the parameters over the full parameter space allowed by the priors. The best-fit parameters for the relations of  $r_{\text{cool}}$  to  $M_{500}$  and to  $r_{500}$  are summarized in Table 7. The best-fit relations for  $M_{500}$  and  $r_{500}$  with  $1\sigma$  uncertainty are shown in Figure 7.

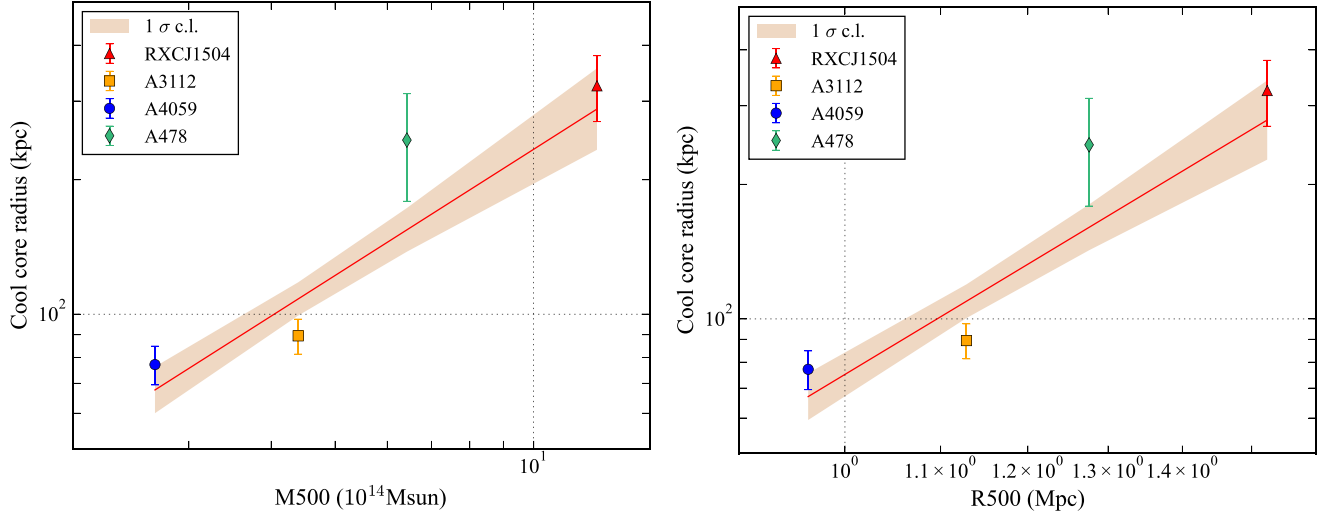


**Figure 7.** Relations of the cool-core radius ( $r_{\text{cool}}$ )– $M_{500}$  and to  $r_{500}$ . Left: the relation between  $r_{\text{cool}}$  and  $M_{500}$ . The red solid line and shaded region show the best-fit relation obtained from the fitting in the log-log space and its  $1\sigma$  uncertainty, respectively. Right: same as the left panel but for the relation between  $r_{\text{cool}}$  and  $r_{500}$ .

**Table 7**  
Best-fit Parameters of the Relation of  $r_{\text{cool}}$  to  $M_{500}$  and to  $r_{500}$

	$r_{\text{cool}}$ vs. $M_{500}$		$r_{\text{cool}}$ vs. $r_{500}$		
$A_M$	$N_M = 10^{A_M}$	$\alpha_M$	$A_r$	$N_r = 10^{A_r}$	$\alpha_r$
$-0.10 \pm 0.04$	$0.79^{+0.08}_{-0.07}$	$0.94 \pm 0.18$	$-0.10 \pm 0.04$	$0.80^{+0.08}_{-0.07}$	$3.12 \pm 0.59$

Based on the analysis with a very limited sample size (i.e., only four clusters), we find that the best-fit relation of the cool-core radius to  $M_{500}$  is consistent with a linear relation (i.e.,  $\alpha_M = 0.94 \pm 0.18$ ). Since  $M_{500}$  is proportional to  $r_{500}^3$ , the best-fit slope for the  $r_{\text{cool}}-r_{500}$  relation is also consistent with this dependency (i.e.,  $\alpha_r = 3.12 \pm 0.59$ ). However, it is difficult to arrive at a robust conclusion regarding these relations due to such a very small sample size. Further study should be conducted to interpret these results robustly. The detailed study of these relations with a larger sample size will be reported in a separate paper (Ng & Ueda 2024, in preparation).

Despite such limitations, here, we attempt to investigate the possible mechanism(s) for the observed relations. If we assume  $r_{\text{cool}} \propto L_X$ , meaning that the size of cool cores depends on the X-ray luminosity of their host galaxy clusters, can we infer a slope for the  $r_{\text{cool}}-M_{500}$  relation? Since the cluster mass  $M_{500}$  was estimated using the luminosity–mass scaling relation from Arnaud et al. (2010;  $L_X \propto M^{1.64}$ ), with the X-ray luminosity in the 0.1–2.4 keV band within  $r_{500}$  being used in the calculation (see Piffaretti et al. 2011), a slope of  $\sim 1.6$  may be expected for the  $r_{\text{cool}}-M_{500}$  relation. Previous studies found that the observed slope for the luminosity–mass scaling relation falls within the range of  $1.3 \sim 2$  (see the review by Giodini et al. 2013 and references therein). Furthermore, the self-similar model predicts a slope of  $4/3$  for the luminosity–mass relation. On the other hand, if  $r_{\text{cool}} \propto t_{\text{cool}}$ ,  $t_{\text{cool}} \propto n^{-1}\sqrt{T}$  may yield a slope of  $1/3$  for the  $r_{\text{cool}}-M_{500}$  relation. However, the best-fit slope is inconsistent with these slopes.

The observed linear relation between  $r_{\text{cool}}$  and  $M_{500}$  indicates that not only baryon physics, such as cooling, heating, and heat transport, is crucial for the formation of cool cores, but also the size of cool cores is linked to the evolution of their host galaxy

clusters. Once the mass of a galaxy cluster increases owing to a cluster merger, the ICM density at the center is expected to increase after the relaxation of merger events. Then, radiative cooling becomes more efficient, leading to the accumulation of a large amount of cool gas in the central region. Since galaxy clusters grow through continuous accretion of material, including cluster mergers, from their surrounding large-scale environments, gas sloshing is expected to take place in cool cores continuously. In fact, this hypothesis is supported by recent comprehensive studies of cool cores (Ueda et al. 2020, 2021). Therefore, the continuous occurrence of gas sloshing may play a crucial role not only in determining the size of cool cores but also in suppressing runaway cooling of the ICM.

AGN feedback is also expected to play a crucial role not only in transporting gas from the central regions to the outer regions but also in contributing significantly to heating the ICM in cool cores. X-ray cavities are commonly observed in cool cores and considered to be generated by AGN activities such as radio jets (e.g., Birzan et al. 2004; Rafferty et al. 2006; Hlavacek-Larrondo et al. 2015; Shin et al. 2016). In fact, the cavity power correlates with the X-ray luminosity in the corresponding regions. Numerical simulations of AGN feedback indicate that the self-regulated feedback of AGN is one of the promising heating sources to explain the observed stability of cool cores (e.g., Gaspari et al. 2011; Yang & Reynolds 2016). Hence, the size of cool cores may also be influenced by AGN feedback. Cool cores may coevolve with their host galaxy clusters.

For the relation between the cool-core radius and a fiducial radius, Vikhlinin et al. (2005) reported that the projected temperature as a function of radius reaches a maximum at

$r \sim 0.1 - 0.2 r_{180}$ . Rasmussen & Ponman (2007) studied the relation between the peak position in the temperature profile (i.e.,  $r_{\text{cool}}$ ) and  $r_{500}$  using a sample of 15 nearby galaxy groups observed with Chandra. Assuming a linear relation, they fitted the data and obtained  $r_{\text{cool}} = (0.20 \pm 0.02)(r_{500}/\text{kpc}) - (46.7 \pm 15.1)\text{kpc}$ . O’Sullivan et al. (2017) also studied the relation between the turnover radius and  $r_{500}$  using a sample of high-richness local galaxy groups, finding that the observed relation in their sample is mostly consistent with that presented by Rasmussen & Ponman (2007). In addition, Rasmussen & Ponman (2007) and O’Sullivan et al. (2017) pointed out that the relation for galaxy groups differs from that observed in a sample of local galaxy clusters (Vikhlinin et al. 2005), suggesting that this discrepancy may be attributed to differences in the physical properties between galaxy clusters and groups. In fact, our best-fit relation between  $r_{\text{cool}}$  and  $r_{500}$  seems to deviate from that observed for galaxy groups. Since galaxy groups have a lower temperature gas compared to galaxy clusters, radiative cooling becomes more efficient owing to emission lines from the metals in the ICM. Additionally, mergers may have a more significant impact on a cool core of the primary galaxy group. Perhaps the  $r_{\text{cool}}-r_{500}$  relation may have a break. Further study is required to arrive at a firm conclusion regarding the similarities and differences in the  $r_{\text{cool}}-r_{500}$  relation between galaxy clusters and groups.

### 5.3. Scaled Radial Profiles of the ICM Thermodynamic Properties

To look deeply into the ICM thermodynamic properties within the cool cores, here we scale the observed radial profiles. These scaled profiles are presented by normalizing the values on the horizontal and the vertical axes by the cool-core radius and the value of each component at the cool-core radius, respectively. Figure 8 shows the scaled radial profile of the ICM temperature. Figure 9 presents the scaled profiles of the other components.

A possible universal form is found in the scaled temperature profiles. To clarify this point, we simultaneously fit the scaled temperature profiles using the same model as that used in Section 4.3 with the MCMC method. In this fitting, we fix  $r_{\text{cool}}$  in Equation (4) at 1.0 since the temperature profile has already been scaled by  $r_{\text{cool}}$ . Instead, we add a new parameter, intrinsic scatter, into the log-likelihood function. Therefore, the log-likelihood function can be expressed as

$$-2 \ln \mathcal{L} = \sum_i \ln(2\pi\sigma_i^2) + \sum_i \frac{[y_i - T(r_i)]^2}{\sigma_i^2}, \quad (9)$$

where  $i$  runs over all annulus in which sample,  $y_i$  and  $T(r_i)$  are the scaled value and the model prediction of the scaled temperature profile in each radial bin, respectively, and  $\sigma_i$  includes the observational uncertainty  $\sigma_{y_i}$  and lognormal intrinsic scatter  $\sigma_{\text{int}}$ ,

$$\sigma_i^2 = \sigma_{y_i}^2 + \sigma_{\text{int}}^2. \quad (10)$$

The  $\sigma_{\text{int}}$  parameter accounts for the intrinsic scatter around the mean relation due to unaccounted errors and/or astrophysics. We continue to use uninformative uniform priors on  $T_{\text{center}}$ ,  $T_{\text{peak}}$ ,  $\alpha_1$ ,  $\alpha_2$ , and  $\ln \sigma_{\text{int}}$  as  $T_{\text{center}} \in (0, 2)$ ,  $T_{\text{peak}} \in (0, 2)$ ,  $\alpha_1 \in (0, 2)$ ,  $\alpha_2 \in (-2, 0)$ , and  $\ln \sigma_{\text{int}} \in (-20, 1)$ . We sample the posterior probability distributions of the parameters over the full parameter space allowed by the priors. The best-fit parameters are summarized in Table 8.

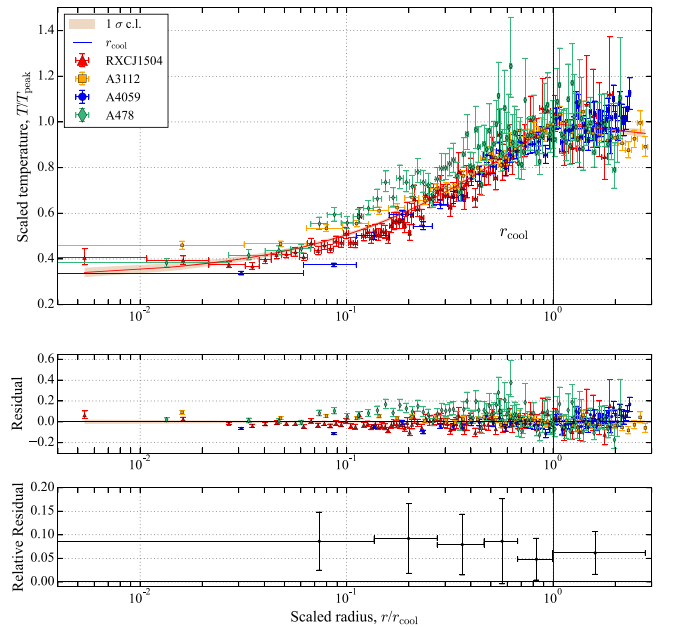


**Figure 8.** Temperature profile of each cluster scaled by  $r_{\text{cool}}$  and  $T_{\text{peak}}$  for the horizontal and the vertical axes, respectively. The red dashed line and shaded region display the best-fit profile and  $1\sigma$  uncertainty, respectively. The blue, vertical solid line indicates  $r_{\text{cool}} = 1$ . The residuals and mean absolute relative residuals are shown in the middle and bottom rows, respectively.

We find that the ratio of the temperature at the center to the peak value is  $0.34 \pm 0.13$ , which is in good agreement with the well-known observational trend in the temperature profiles of cool-core clusters (e.g., Sanderson et al. 2006; Hudson et al. 2010; Simionescu et al. 2011). The slopes of the model for the regions inside and outside the cool cores are measured at  $\alpha_1 = 0.78 \pm 0.12$  and  $\alpha_2 = -0.14 \pm 0.10$ , respectively. The intrinsic scatter  $\sigma_{\text{int}}$  is obtained at  $3.25_{-0.79}^{+1.04}\%$ .

A possible universal form in the temperature profiles scaled by a fiducial radius ( $r_{2500}$  or  $r_{500}$ ) within cool cores has been proposed (e.g., Allen et al. 2001; Sanderson et al. 2006). On the other hand, Vikhlinin et al. (2005) and Hudson et al. (2010) reported no such universal form. Our results indicate a possible universal form in the scaled temperature profile. Since all cool cores in the sample are classified into strong cool cores (Hudson et al. 2010), such a universal form may be observed in strong cool cores only. Additionally, we have scaled the temperature profiles by the cool-core radius rather than a fiducial radius like  $r_{500}$ . It is possible that the cool-core radius is a more appropriate factor than a fiducial radius for scaling the radial profiles of the ICM thermodynamic properties, as indicated by the observed intrinsic scatter. The ratio of  $r_{\text{cool}}-r_{500}$  varies within our sample (see Table 6), emphasizing the significance of the chosen radius for scaling in revealing a universal form in the temperature profile.

To investigate possible universal forms seen in the other components, we also scale the radial profiles using the same manner as that for the scaled temperature profiles. Figure 9 shows the scaled radial profiles of the ICM electron number density, pressure, entropy, and radiative cooling time. In contrast to the scaled temperature profiles, we find that there is no universal form in the scaled profiles within the cool cores. The values of each profile at the center are highly scattered, suggesting that the ICM temperature is likely the most fundamental factor for characterizing cool cores. However, further studies are required to reveal possible universal forms in

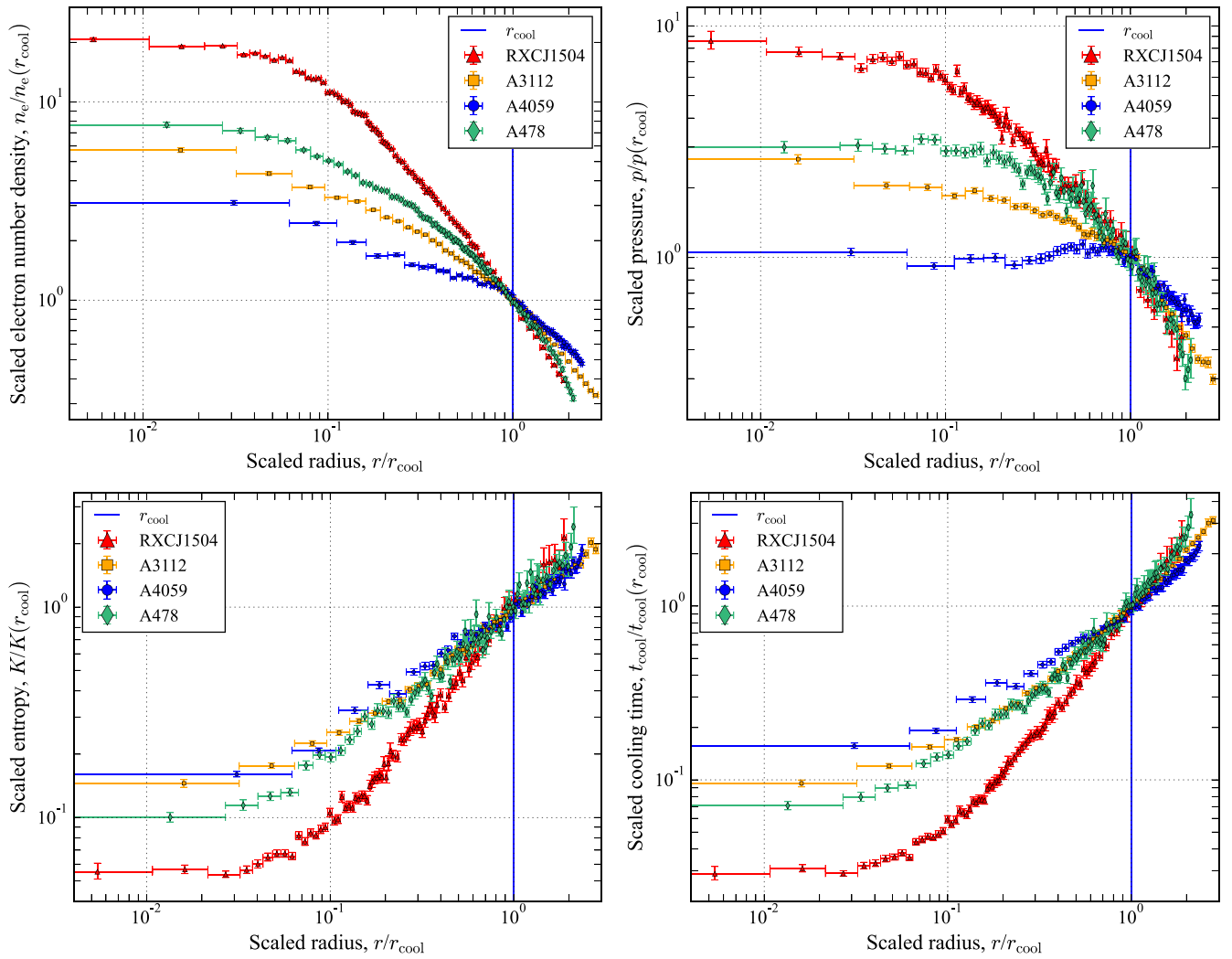


**Figure 9.** Scaled radial profiles of the ICM electron number density (top left), pressure (top right), entropy (bottom left), and radiative cooling time (bottom right) in the sample. The radial profiles are normalized in the same manner as in Figure 8.

**Table 8**

Best-fit Parameters Derived from the Simultaneous Fitting of the Scaled Temperature Profiles

$T_{\text{center}}$	$T_{\text{peak}}$	$r_{\text{cool}}$	$\alpha_1$	$\alpha_2$	$\sigma_{\text{int}}(\%)$
$0.34 \pm 0.13$	$0.99 \pm 0.03$	1 (fixed)	$0.78 \pm 0.12$	$-0.14 \pm 0.10$	$3.25^{+1.04}_{-0.79}$

the radial profiles of the ICM thermodynamic properties. An approach involving forward model fitting will be useful for conducting a simultaneous analysis of the ICM temperature and density profiles (e.g., Umetsu et al., 2022).

In the region outside the cool cores, a universal form is found in the scaled entropy profile. Such a universal form is known as the universal entropy profile (Voit et al. 2005). However, in the region inside the cool cores, the scaled entropy profiles for our sample start varying toward the cluster center, indicating that the cool-core radius is influenced by the interplay between cooling and heating processes.

#### 5.4. Analysis of Thermodynamic Perturbations

It has been studied that thermodynamic perturbations in the ICM are a good proxy for examining gas motions, including turbulence (e.g., Gaspari et al. 2014; Churazov et al. 2016; Hofmann et al.

2016; Ueda et al. 2018; Zhuravleva et al. 2018; Kitayama et al. 2020; Ueda et al. 2021; Zhuravleva et al. 2023). Gaspari et al. (2014) presented that entropy perturbations in the ICM can be used to infer one-dimensional Mach numbers of turbulence ( $\mathcal{M}_{1D}$ ), assuming that pressure perturbations in the ICM are negligible. Following Gaspari et al. (2014), Hofmann et al. (2016) measured pressure and entropy perturbations in the ICM, and estimated  $\mathcal{M}_{1D}$  within the cool cores in a sample of 33 galaxy clusters.

Motivated by Gaspari et al. (2014) and Hofmann et al. (2016), we investigate thermodynamic perturbations in the ICM to constrain gas motions in the cool cores in our sample. We have measured the residuals and mean absolute relative residuals between the observed and the best-fit profiles (see the middle and bottom panels of Figures 2–5), which can be converted into average fractional perturbations. We calculate the average fractional perturbations in the ICM thermodynamic properties within the cool cores, as summarized in Table 9. Our

**Table 9**  
Average Fractional Perturbations in the Temperature, Electron Number Density, Pressure, and Entropy Profiles within the Cool Cores

Cluster	$\langle  dT /T \rangle$	$\langle  dn /n \rangle$	$\langle  dP /P \rangle$	$\langle  dK /K \rangle$
RXCJ1504.1-0248	$0.047 \pm 0.041$	$0.019 \pm 0.015$	$0.046 \pm 0.044$	$0.051 \pm 0.044$
A3112	$0.021 \pm 0.017$	$0.029 \pm 0.051$	$0.032 \pm 0.060$	$0.030 \pm 0.030$
A4059	$0.046 \pm 0.035$	$0.028 \pm 0.019$	$0.031 \pm 0.027$	$0.060 \pm 0.043$
A478	$0.075 \pm 0.066$	$0.015 \pm 0.010$	$0.073 \pm 0.060$	$0.077 \pm 0.069$

results are consistent with those measured by Hofmann et al. (2016) for their sample. In particular, the average fractional perturbations in the ICM pressure in our sample is lower than 0.15, which agrees with their measurements ( $0.09 \pm 0.06$ ). Thus, the observed perturbations are nearly isobaric. Therefore, similar to Hofmann et al. (2016), the entropy perturbations in the ICM can be used to infer  $\mathcal{M}_{1D}$ .

Assuming that the perturbations are isobaric, the observed entropy perturbations can directly be converted into values of  $\mathcal{M}_{1D}$ . A478 exhibits a slightly larger  $\mathcal{M}_{1D}$  with  $0.077 \pm 0.069$ , while the inferred values of  $\mathcal{M}_{1D}$  are comparable in the sample. Thus, the corresponding three-dimensional Mach numbers ( $\mathcal{M}_{3D}$ ) of the sample are lower than  $\mathcal{M}_{3D} < 0.25$ , which is significantly lower than unity and is consistent with those measured by the previous studies (Hofmann et al. 2016; Hitomi Collaboration et al. 2018; Ueda et al. 2021). We expect that XRISM will be able to achieve direct measurements of the turbulent velocity for our sample (Tashiro et al. 2018). Additionally, the Athena X-ray Observatory will provide us with a great opportunity to measure turbulent velocities in cool cores (Nandra et al. 2013; Barcons et al. 2017).

## 6. Summary and Conclusions

In this paper, we have conducted a detailed study of the radial profiles of the ICM thermodynamic properties in cool-core systems in a sample of four galaxy clusters (RXCJ1504.1-0248, A3112, A4059, and A478), using archival X-ray data from the Chandra X-ray Observatory. The goal of this study was to observe the characteristics of the cool cores in the sample and explore mechanisms to generate the observed characteristics. To this end, we have measured the turnover radius in the radial profile of the ICM temperature and defined the cool-core radius as the turnover radius. We have also studied the thermodynamic properties of the ICM within the cool-core radius and the relation between the cool-core radius and the cluster mass. The main conclusions of this paper are summarized as follows:

1. Since cool cores are characterized by a significant drop in the ICM temperature toward the cluster center, we defined the cool-core radius as the turnover radius in the ICM temperature profile, allowing us to study the ICM thermodynamic properties in the regions inside and outside the cool cores. We found no apparent feature at the cool-core radius in the radial profiles of the ICM electron density, pressure, entropy, and radiative cooling time. These results indicate that the boundary between inside and outside cool cores is primarily identified in the temperature profile, suggesting that the ICM temperature is the most fundamental factor for characterizing cool cores.
2. In our sample, the radiative cooling time of the ICM at the cool-core radius exceeds 10 Gyr, with RXCJ1504.1-0248 exhibiting a radiative cooling time of  $32_{-11}^{+5}$  Gyr at its cool-core radius. Such a long timescale indicates that

not only radiative cooling but also additional mechanisms may be required to explain the observed properties. Gas sloshing is possible to displace cool gas generated by radiative cooling away from the center and induce mixing between such cool gas and the ambient hot gas in the outer region, leading to a temperature drop.

3. Based on the analysis with a very limited sample size, we found that the best-fit relation between the cool-core radius and the cluster mass  $M_{500}$  in our sample is consistent with a linear relation, which may deviate from other expected relations. Our findings suggest that cool cores are linked to the evolution of galaxy clusters. Cool cores may coevolve with their host galaxy clusters. Since the cluster mass increases owing to mergers, which in turn induce gas sloshing, it is plausible that gas sloshing plays a significant role in the evolution of cool cores.
4. A possible universal form in the temperature profiles scaled by the cool-core radius is found in the cool cores in our sample. Such a universal form has been presented in scaled temperature profiles by a fiducial radius such as  $r_{500}$ . Our result is broadly in agreement with the previous findings. However, the scaled profiles of the other components within the cool cores are highly scattered, indicating that there is no universal form.
5. The one-dimensional Mach numbers of turbulence ( $\mathcal{M}_{1D}$ ) in the cool cores in the sample are constrained by analyzing the entropy perturbations in the ICM. The inferred  $\mathcal{M}_{3D}$  is significantly lower than unity, suggesting that subsonic gas motions are dominant in the cool cores.

## Acknowledgments

We are grateful to the anonymous referee for the helpful and constructive comments. We thank Keiichi Umetsu for the fruitful discussions. We also thank H.-Y. Karen Yang for the helpful comments. The scientific results of this paper are based in part on data obtained from the Chandra Data Archive.<sup>10</sup> S.U. acknowledges the support from the National Science and Technology Council of Taiwan (NSTC 111-2811-M-007-008 and 111-2112-M-001-026-MY3). We thank the ASIAA Summer Student Program 2019 for its hospitality and for providing us with an opportunity to launch the project.

*Facility:* CXO.

*Software:* Astropy (Astropy Collaboration et al. 2013, 2018), CIAO (Fruscione et al. 2006), XSPEC (Arnaud 1996).

## Appendix A

### Region Selection for X-Ray Spectral Analysis

Here, we summarize detailed information regarding the region selection and radial bin sizes of the regions for the X-ray spectral analysis in Table 10.

<sup>10</sup> >doi:10.25574/cdc.223

**Table 10**

Summary of Our Region Selection for the X-Ray Spectral Analysis: Region Interval, Region Range, the Number of Regions, and the Maximum Size for Our Region Selection

Cluster	Region Interval (arcsec) <sup>a</sup>	Region Range (arcsec)	Number of Regions	Maximum Size (arcsec) <sup>b</sup>
RXCJ1504.1-0248	1	0–3	3	180
	0.5	3–20	34	
	1	20–36	16	
	2	36–60	12	
	5	60–90	6	
	10	90–180	9	
A3112	2	0–60	30	180
	5	60–100	8	
	10	100–180	8	
A4059	5	0–5	1	192
	4	5–25	5	
	3	25–160	45	
	4	160–192	8	
A478	4	0–4	1	320
	2	4–110	53	
	4	110–210	25	
	10	210–320	11	

**Notes.**

<sup>a</sup> Radial bin size between the inner and outer major axes of each elliptical annulus region.

<sup>b</sup> Size at the outermost region in our region selection.

### Appendix B Radial Profiles of the ICM Metal Abundance

Here, we show the radial profiles of the ICM metal abundance for the sample in Figure 10. We find that the


ICM metal abundance in A3112 starts slightly decreasing at  $\sim 15$  kpc toward the center, and A4059 also exhibits a decrease of the ICM metal abundance from  $\sim 20$  kpc to the center, which is consistent with that measured by Choi et al. (2004).

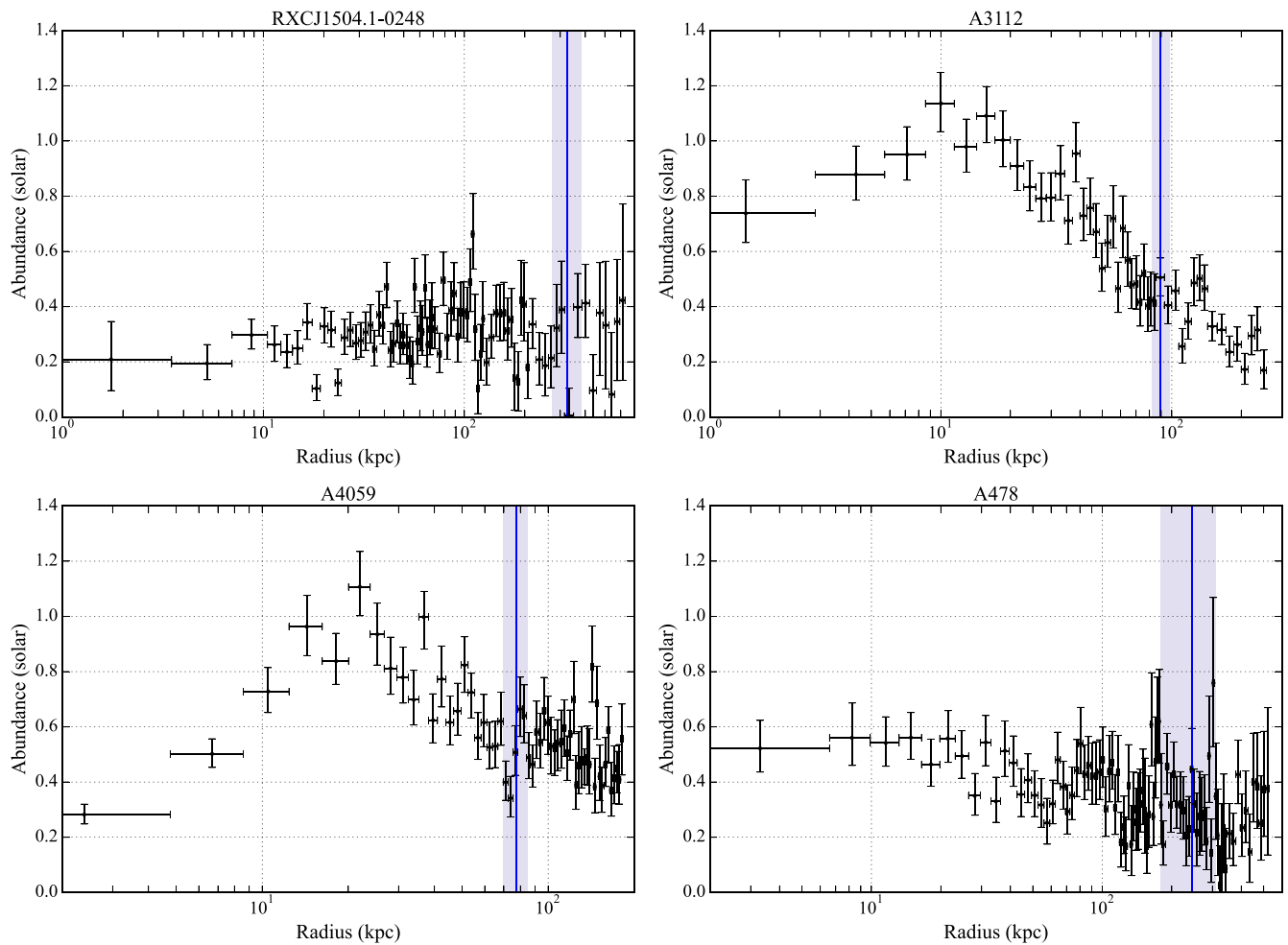


**Figure 10.** Radial profiles of the ICM metal abundance: RXCJ1504.1-0248 (top left), A3112 (top right), A4059 (bottom left), and A478 (bottom right). The blue, vertical solid line and shaded region correspond to the cool-core radius and  $1\sigma$  uncertainty for each cluster.

### ORCID iDs

FanLam Ng  <https://orcid.org/0000-0003-4195-6300>

Shutaro Ueda  <https://orcid.org/0000-0001-6252-7922>

### References

- Allen, S. W., Schmidt, R. W., & Fabian, A. C. 2001, *MNRAS*, **328**, L37
- Anders, E., & Grevesse, N. 1989, *GeCoA*, **53**, 197
- Arnaud, K. A. 1996, in ASP Conf. Ser. 101, *Astronomical Data Analysis Software and Systems V*, ed. G. H. Jacoby & J. Barnes (San Francisco, CA: ASP), 17
- Arnaud, M., Pratt, G. W., Piffaretti, R., et al. 2010, *A&A*, **517**, A92
- Ascasibar, Y., & Markevitch, M. 2006, *ApJ*, **650**, 102
- Astropy Collaboration, Price-Whelan, A. M., Sipőcz, B. M., et al. 2018, *AJ*, **156**, 123
- Astropy Collaboration, Robitaille, T. P., Tollerud, E. J., et al. 2013, *A&A*, **558**, A33
- Barcons, X., Barret, D., Decourchelle, A., et al. 2017, *AN*, **338**, 153
- Barnes, D. J., Vogelsberger, M., Kannan, R., et al. 2018, *MNRAS*, **481**, 1809
- Bauer, F. E., Fabian, A. C., Sanders, J. S., Allen, S. W., & Johnstone, R. M. 2005, *MNRAS*, **359**, 1481
- Birzan, L., Rafferty, D. A., McNamara, B. R., Wise, M. W., & Nulsen, P. E. J. 2004, *ApJ*, **607**, 800
- Böhringer, H., Burwitz, V., Zhang, Y.-Y., Schuecker, P., & Nowak, N. 2005, *ApJ*, **633**, 148
- Bulbul, G. E., Smith, R. K., Foster, A., et al. 2012, *ApJ*, **747**, 32
- Cavaliere, A., & Fusco-Femiano, R. 1976, *A&A*, **49**, 137
- Cavaliere, A., & Fusco-Femiano, R. 1978, *A&A*, **70**, 677
- Chen, Y., Reiprich, T. H., Böhringer, H., Ikebe, Y., & Zhang, Y. Y. 2007, *A&A*, **466**, 805
- Choi, Y.-Y., Reynolds, C. S., Heinz, S., et al. 2004, *ApJ*, **606**, 185
- Churazov, E., Arevalo, P., Forman, W., et al. 2016, *MNRAS*, **463**, 1057
- Ettori, S. 2000, *MNRAS*, **318**, 1041
- Ezer, C., Bulbul, E., Nihal Ercan, E., et al. 2017, *ApJ*, **836**, 110
- Fabian, A. C. 1994, *ARA&A*, **32**, 277
- Foreman-Mackey, D., Hogg, D. W., Lang, D., & Goodman, J. 2013, *PASP*, **125**, 306
- Foster, A. R., Ji, L., Smith, R. K., & Brickhouse, N. S. 2012, *ApJ*, **756**, 128
- Fruscione, A., McDowell, J. C., Allen, G. E., et al. 2006, *Proc. SPIE*, **6270**, 62701V
- Garmire, G. P., Bautz, M. W., Ford, P. G., & Nousek, J. A., Jr 2003, *Proc. SPIE*, **4851**, 28
- Gaspari, M., Churazov, E., Nagai, D., Lau, E. T., & Zhuravleva, I. 2014, *A&A*, **569**, A67
- Gaspari, M., Melioli, C., Brighenti, F., & D’Ercole, A. 2011, *MNRAS*, **411**, 349
- Giacintucci, S., Markevitch, M., Brunetti, G., Cassano, R., & Venturi, T. 2011, *A&A*, **525**, L10
- Giodini, S., Lovisari, L., Pointecouteau, E., et al. 2013, *SSRv*, **177**, 247
- Goodman, J., & Weare, J. 2010, *CAMCS*, **5**, 65
- Henning, J. W., Gantner, B., Burns, J. O., & Hallman, E. J. 2009, *ApJ*, **697**, 1597
- HI4PI Collaboration, Ben Bekhti, N., Flöer, L., et al. 2016, *A&A*, **594**, A116
- Hitomi Collaboration, Aharonian, F., Akamatsu, H., et al. 2018, *PASJ*, **70**, 9
- Hlavacek-Larrondo, J., & Fabian, A. C. 2011, *MNRAS*, **413**, 313
- Hlavacek-Larrondo, J., McDonald, M., Benson, B. A., et al. 2015, *ApJ*, **805**, 35
- Hofmann, F., Sanders, J. S., Nandra, K., Clerc, N., & Gaspari, M. 2016, *A&A*, **585**, A130

- Huang, Z., & Sarazin, C. L. 1998, *ApJ*, 496, 728
- Hudson, D. S., Mittal, R., Reiprich, T. H., et al. 2010, *A&A*, 513, A37
- Kaastra, J. S., Tamura, T., Peterson, J. R., et al. 2004, *A&A*, 413, 415
- Keshet, U. 2012, *ApJ*, 753, 120
- Keshet, U., Raveh, I., & Ghosh, A. 2023, *MNRAS*, 522, 4991
- Kitayama, T., Ueda, S., Akahori, T., et al. 2020, *PASJ*, 72, 33
- Laganá, T. F., Durret, F., & Lopes, P. A. A. 2019, *MNRAS*, 484, 2807
- Markevitch, M. 2007, arXiv:0705.3289
- McDonald, M., Gaspari, M., McNamara, B. R., & Tremblay, G. R. 2018, *ApJ*, 858, 45
- McDonald, M., McNamara, B. R., Voit, G. M., et al. 2019, *ApJ*, 885, 63
- McDonald, M., Veilleux, S., Rupke, D. S. N., Mushotzky, R., & Reynolds, C. 2011, *ApJ*, 734, 95
- Mernier, F., de Plaa, J., Lovisari, L., et al. 2015, *A&A*, 575, A37
- Molendi, S., & Pizzolato, F. 2001, *ApJ*, 560, 194
- Nandra, K., Barret, D., Barcons, X., et al. 2013, arXiv:1306.2307
- Naor, Y., & Keshet, U. 2020, *ApJ*, 895, 143
- Nulsen, P. E. J., Powell, S. L., & Vikhlinin, A. 2010, *ApJ*, 722, 55
- O’Dea, C. P., Baum, S. A., Privon, G., et al. 2008, *ApJ*, 681, 1035
- O’Sullivan, E., Ponman, T. J., Kolokythas, K., et al. 2017, *MNRAS*, 472, 1482
- Ota, N., Onzuka, K., & Masai, K. 2013, *PASJ*, 65, 47
- Peterson, J. R., & Fabian, A. C. 2006, *PhR*, 427, 1
- Peterson, J. R., Paerels, F. B. S., Kaastra, J. S., et al. 2001, *A&A*, 365, L104
- Piffaretti, R., Arnaud, M., Pratt, G. W., Pointecouteau, E., & Melin, J. B. 2011, *A&A*, 534, A109
- Pointecouteau, E., Arnaud, M., Kaastra, J., & de Plaa, J. 2004, *A&A*, 423, 33
- Rafferty, D. A., McNamara, B. R., Nulsen, P. E. J., & Wise, M. W. 2006, *ApJ*, 652, 216
- Rasmussen, J., & Ponman, T. J. 2007, *MNRAS*, 380, 1554
- Reiprich, T. H., & Böhringer, H. 2002, *ApJ*, 567, 716
- Reynolds, C. S., Casper, E. A., & Heinz, S. 2008, *ApJ*, 679, 1181
- Sanderson, A. J. R., Finoguenov, A., & Mohr, J. J. 2005, *ApJ*, 630, 191
- Sanderson, A. J. R., Ponman, T. J., & O’Sullivan, E. 2006, *MNRAS*, 372, 1496
- Santos, J. S., Rosati, P., Tozzi, P., et al. 2008, *A&A*, 483, 35
- Santos, J. S., Tozzi, P., Rosati, P., & Böhringer, H. 2010, *A&A*, 521, A64
- Sayers, J., Czakon, N. G., Mantz, A., et al. 2013, *ApJ*, 768, 177
- Shin, J., Woo, J.-H., & Mulchaey, J. S. 2016, *ApJS*, 227, 31
- Shitanishi, J. A., Pierpaoli, E., Sayers, J., et al. 2018, *MNRAS*, 481, 749
- Simionescu, A., Allen, S. W., Mantz, A., et al. 2011, *Sci*, 331, 1576
- Smith, R. K., Brickhouse, N. S., Liedahl, D. A., & Raymond, J. C. 2001, *ApJL*, 556, L91
- Su, Y., Zhang, Y., Liang, G., et al. 2020, *MNRAS*, 498, 5620
- Sun, M., Jones, C., Murray, S. S., et al. 2003, *ApJ*, 587, 619
- Takizawa, M., Sarazin, C. L., Blanton, E. L., & Taylor, G. B. 2003, *ApJ*, 595, 142
- Tamura, T., Kaastra, J. S., Peterson, J. R., et al. 2001, *A&A*, 365, L87
- Tashiro, M., Maejima, H., Toda, K., et al. 2018, *Proc. SPIE*, 10699, 1069922
- Ueda, S., Ichinohe, Y., Molnar, S. M., Umetsu, K., & Kitayama, T. 2020, *ApJ*, 892, 100
- Ueda, S., Kitayama, T., & Dotani, T. 2017, *ApJ*, 837, 34
- Ueda, S., Kitayama, T., Oguri, M., et al. 2018, *ApJ*, 866, 48
- Ueda, S., Umetsu, K., Ng, F., et al. 2021, *ApJ*, 922, 81
- Umetsu, K., Ueda, S., Hsieh, B.-C., et al. 2022, *ApJ*, 934, 169
- Vikhlinin, A., Burenin, R. A., Ebeling, H., et al. 2009, *ApJ*, 692, 1033
- Vikhlinin, A., Kravtsov, A., Forman, W., et al. 2006, *ApJ*, 640, 691
- Vikhlinin, A., Markevitch, M., Murray, S. S., et al. 2005, *ApJ*, 628, 655
- Voigt, L. M., Schmidt, R. W., Fabian, A. C., Allen, S. W., & Johnstone, R. M. 2002, *MNRAS*, 335, L7
- Voit, G. M., Kay, S. T., & Bryan, G. L. 2005, *MNRAS*, 364, 909
- Wang, L., Tozzi, P., Yu, H., Gaspari, M., & Ettori, S. 2023, *A&A*, 674, A102
- Yang, H.-Y. K., & Reynolds, C. S. 2016, *ApJ*, 818, 181
- Zhuravleva, I., Allen, S. W., Mantz, A., & Werner, N. 2018, *ApJ*, 865, 53
- Zhuravleva, I., Chen, M. C., Churazov, E., et al. 2023, *MNRAS*, 520, 5157
- ZuHone, J. A., Markevitch, M., & Johnson, R. E. 2010, *ApJ*, 717, 908